INVESTIGATION OF SUBMERGED FRICTION

STIR WELDING OF MARINE-GRADE ALUMINUM ALLOY

by

Emad Eldin Mohammed Kishta

A Thesis Presented to the Faculty of the
American University of Sharjah
College of Engineering
in Partial Fulfillment
of the Requirements
for the Degree of

Master of Science in
Mechanical Engineering

Sharjah, United Arab Emirates

January 2014

Approval Signatures

We, the undersigned, approve the Master's Thesis of Emad Eldin Kishta.

Thesis Title: Investigation of Submerged Friction Stir Welding of Marine-grade Aluminum Alloy.

Signature	**Date of Signature** (dd/mm/yyyy)
_____	_____
Dr. Basil Darras Assistant Professor, Department of Mechanical Engineering Thesis Advisor	
_____	_____
Dr. Farid Abed Associate Professor, Department of Civil Engineering Thesis Co-Advisor	
_____	_____
Dr. Shivakumar Ranganathan Assistant Professor, Department of Mechanical Engineering Thesis Committee Member	
_____	_____
Dr. Mamoun Abdel-Hafez Associate Professor, Department of Mechanical Engineering Thesis Committee Member	
_____	_____
Dr. Noha Hussein Associate Professor, Department of Industrial Engineering Thesis Committee Member	
_____	_____
Dr. Essam Wahba Interim Head, Department of Mechanical Engineering	
_____	_____
Dr. Hany El-Kadi Associate Dean, College of Engineering	
_____	_____
Dr. Leland Blank Dean, College of Engineering	
_____	_____
Dr. Khaled Assaleh Director of Graduate Studies	

Acknowledgements

In the name of *Allah*, the most gracious and most merciful.

First, I am most grateful to *Allah* for granting me the power and will to carry on and complete this research. In addition, I would like to express my appreciation and gratitude to Dr. Basil Darras, my thesis advisor, for his selfless and patient guidance and support throughout this research. I would also like to thank Dr. Farid Abed, my thesis co-advisor, for teaching me everything I know about finite element modeling and for generously giving me his time to guide and assist me throughout the numerical modeling portion of the research.

I also wish to thank Eng. Salman Pervaiz for his technical support in addition to teaching and aiding me in using the lab equipment. Many thanks go to Mr. Ricardo De Jesus and Mr. Ronald Almirez for their valuable assistance in the experimental work. My thanks also go the American University of Sharjah and especially to the Department of Mechanical Engineering for supplying the labs and equipment used in this research. Furthermore, I would like to thank Ms. Salwa Mohamed for her guidance throughout this research and during my graduate studies. Finally, I would like to express my sincere thanks and gratitude to my family and friends for the unconditional support.

To my beloved mother and late father;

may Allah have mercy on him

Abstract

Friction stir welding is a newly developed welding technique utilized to weld lightweight alloys, such as aluminum alloys. Due to its low melting temperature, welding aluminum has been always challenging using conventional techniques. Friction stir welding can be controlled by different parameters like rotational speed, feed rate and welding medium. In this research, submerged friction stir welding of marine grade aluminum alloy 5083 is investigated. The study is divided into two parts, experimental and numerical investigations. In the experimental part, the effect of different welding parameters on thermal histories, tensile properties and microstructural properties are studied. The numerical part is a finite element modeling of the process to predict the changes in thermal profiles and material properties as the welding parameters are changed. The results of this study show that submerging highly affected the thermal histories and thus the microstructural and mechanical properties of the welded alloy. Controlling both the rotational speed and the feed rate found to be crucial to successfully friction stir weld aluminum and achieving good mechanical properties. The finite element model successfully predicted the thermal profile generated by friction stir welding under different parameters.

Table of Contents

List of Figures

List of Tables

Chapter 1 : Introduction

1.1 Problem Statement and Motivation

As welding is one of the most commonly used processes in the industry, achieving a high quality weld has become a goal several researchers thrive to achieve. Plenty of welding techniques were developed throughout the years; however, welding aluminum and its alloys still seem to be problematic due to its high thermal conductivity and relatively low melting temperature. In addition, some applications require the welding to be done underwater, such as repairing underwater pipelines, marine platforms, ships and other marine engineering projects. This may be possible using the conventional welding techniques like arc welding, but it is also considered a very difficult and dangerous technique as it requires the welder to work with electric equipment underwater. Both of these problematic welding cases can be solved using the newly developed welding technique called friction stir welding.

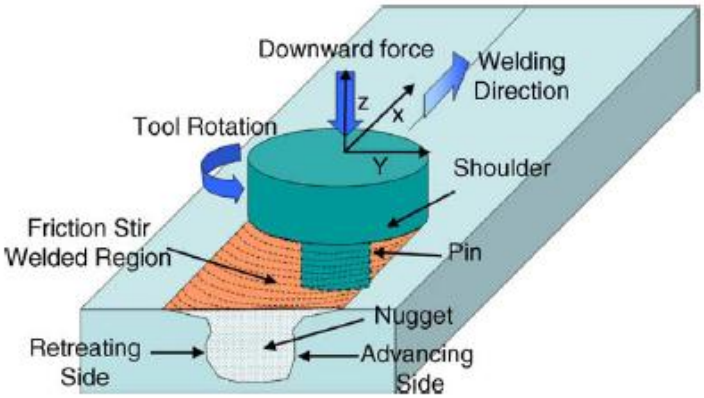

Figure 1.1 - Schematic drawing of friction stir welding [2]

Friction stir welding (FSW) was invented by the Welding Institute in 1991 [1]. FSW is a technique wherein two work pieces are clamped together, and a specially designed rotating tool is used to weld the two pieces together as illustrated in Figure 1.1 [2]. The rotating tool, which consists of a shoulder and a pin, applies the force and heat produced by the friction on the work piece. The friction causes the temperature of the work piece to increase to an extent where the material becomes soft but still not molten. After that, the rotation of the tool stirs the material and causes it to flow

plastically; this is considered a deformation at a temperature under the melting temperature of the material causing various changes in its properties and microstructure [3, 4].

This newly developed welding technique can be used effectively to weld aluminum alloys as the solid state welding occurs at a relatively low temperature compared to the other conventional welding techniques. Moreover, friction stir welding can be performed easily underwater using the same set up used to weld samples in air. This gives friction stir welding an advantage over other welding techniques which tend to be challenging when considering the previous mentioned cases.

During the process, several changes occur in the mechanical properties and microstructure of the material due to plastic deformation. These changes in properties are affected by the welding conditions, such as rotational speed, feed rate and welding medium. Given the great potential of friction stir welding, this project is dedicated to find the relations between the changes in mechanical properties and microstructure and the weld parameters. The study aims at finding the optimum welding parameters to weld aluminum alloy 5083 underwater and developing a numerical model to further investigate the process.

1.2 Objective and Scope of Work

The aim of this project is to investigate the effects of weld parameters on submerged FSW and their effects on the mechanical properties and microstructure of the material. The input parameters that are taken into consideration are the rotational speed, the feed rate and the thermal boundaries. On the other hand, the properties of interest in this study are the yield strength, ultimate tensile strength, ductility and hardness of the weld. The objectives of this project are to be achieved through performing the following tasks:

1- Welding marine-grade 5083 aluminum alloy samples using different rotational speeds and feed rates while recording the thermal profile and the power consumption during the process.
2- Performing tensile test on the welded samples and plotting the stress strain curve to find the mechanical properties of the weld.

3- Taking microscopic images of the welded samples to study the effect of submerged friction stir welding on the microstructure of the material.
4- Developing a finite element model to predict the effects of welding parameters on the welded material and experimentally validate this model.

Whereas, the methodology used to achieve these objectives is as follows: first, a literature review on the topic is done to study what has been achieved so far. The literature review is conducted throughout the whole project period to compare the results and stay updated on the developments occurring in the studied field. The second stage in the investigation is the experimental process, which is the base of this study. The experimental process is divided into two parts. The first part is the welding process where the data recorded is the thermal profile and the power consumption during the process. The second part of the experimental work includes the testing of the samples, which contains the tensile testing and the microscopic testing. Last but not least, the project is concluded by developing a finite element model of the process. This model is based on the experimental work that was previously conducted and may require more experimental work to be validated.

1.3 Thesis Outline

The framework of the current thesis is as shown below:

- Chapter 1: Introduction of the thesis including problem statement, historical background, scope of work, methodology and objectives.
- Chapter 2: Literature review and previous findings on friction stir welding, submerged friction stir welding, marine grade aluminum alloy 5083 and numerical modeling of friction stir welding.
- Chapter 3: Specifications and details about the material, tools and equipment used in this study in addition to the experimental procedure and process parameters.
- Chapter 4: Results and discussion of the effects of friction stir welding on temperature profiles, power consumption, tensile properties and microstructure.
- Chapter 5: Finite element analysis of friction stir welding including model description, validation and results.

- Chapter 6: The conclusion chapter that summarizes the findings of this research in addition to suggesting recommendations and future work that can further enhance the process.

Chapter 2 : Background

2.1 Friction Stir Welding

As mentioned earlier, friction stir welding was developed in 1991 to weld what was referred to as non-weldable alloys, such as 2xxx and 7xxx series aluminum alloys [2]. It should be noted that these alloys are, in fact, not impossible to weld using techniques other than friction stir welding; however, the results of other techniques are very poor. The welded samples exhibit a significant loss in mechanical properties which makes them unreliable. Other welding techniques, such as resistance welding, were suggested; nonetheless, due to their high cost, friction stir welding stand solely as the best welding option for these alloys.

As a relatively new process, various studies were done on friction stir welding. Studies include the effects of welding parameters like rotational speed and feed rate, effects of tool geometries, defects formulations and other related matters. Most of the studies conducted are concerned with friction stir welding performed in air, while a fewer papers focused on submerged friction stir welding.

A study done by McQueen et al. [5] investigated the effect of friction stir welding on aluminum alloy 6065 in terms of mechanical properties and microstructure. The weld was done at a rotational speed of 1800 rpm and a feed rate of 15 mm/s; the tool was placed at an angle of 3° with respect to the welded plate. The study indicates that the tensile strength of the weld is close to 90% of the unprocessed material, and the yield strength is almost the same as that of the unprocessed material. The only unsatisfying result in McQueen et al.'s study is that the ductility decreased to below 50% of the unprocessed alloy. In another study by Lee et al. [6], aluminum alloy 356 samples were friction stir welded at 1600 rpm rotational speed, a feed rate ranging between 87 to 342 mm/min and an angle of 3° with respect to the welded plate. The results show that the welded zone has transverse ultimate yield strength similar to that of the base material; in addition, the longitudinal ultimate tensile strength of the welded material improved by 20% compared to the base material. It was also noted that all the specimens were fractured at the unaffected base material rather than the welded material.

In addition to McQueen et al.'s studies, Klobčar et al. [7] studied the effect of heat input in friction stir welding by varying the rotational speed and feed rate. aluminum alloy 5083 was used as the material of this study. At the microscopic level, the higher heat input achieved larger grains compared to samples with lower heat input. The samples welded at relatively high and low heat input achieved a slightly lower tensile strength; whereas, the samples that welded at medium heat input achieved higher tensile strength compared to base material. The sample welded with low heat input attained the highest hardness compared to the other samples while welding at high heat input resulted in the lowest hardness.

Sutton et al. [8] investigated the microstructure of friction stir welded 2024-T3 aluminum and its variation in the stir zone. The weld was done at a rotational speed of 360 rpm and a feed rate of 3.3 mm/s using a tool with a 23 mm diameter shoulder and an 8.2 diameter pin. Different etching techniques were used in the study to obtain high-contrast images of each FSW sample. Furthermore, Mixed-mode I/II monotonic fracture experiments were conducted to study the microstructure effect on the fracture path of the FSW samples. It was found that the microstructure of the FSW samples is non-uniform and alternating between hard particle-rich and hard particle-poor regions. It was also found that the fracture path is affected by the microstructure and tends to follow high particle density regions. The results of this study come in agreement with Schneider et al.'s study [9] where TEM imagining of FSW aluminum alloy 2915-T81 was used. A variety of grain diameters were found in the stir zone; the majority of the sizes found landed between 4 to 22 microns.

An experimental and numerical study by Xu et al. [10] focused on the effect of welding parameters and tool shoulder diameter on the thermal histories of friction stir welded aluminum magnesium alloy 5083-H116. The study found that as the feed rate of the tool increases, the heat generated by the shoulder decreases and the heat generated by the pin increases. The heat generated by the shoulder was found to be also affected by the diameter of the shoulder; an increase in the shoulder diameter causes an increase in the heat generated. The shoulder : pin heat generation ratio revealed in the study ranges between 60% : 40% to 30% : 70% depending on the welding parameters discussed earlier.

The microhardness of friction stir welded samples is studied by Jones et al. [11]. 2024-T351 aluminum alloy was used as a base material in this study; the microhardness of the unprocessed material was found to be 135 HV. After being welded, it is noticed that the hardness at the nugget zone fluctuated in the range of 120-130 HV and decreased to 100 HV as it moved away from the weld zone. Finally, the hardness increases up to 135 HV as it moves closer to the base material at the edges of the heat affected zone.

Some studies focused on the effects of tool geometry on FSW [12-15]. Fujii et al. [15] studied the relation between tool geometries, and mechanical properties and microstructure of different aluminum alloys in FSW. The three types of FSW tools considered in the study were column without threads, column with threads and triangular prism shape. Three aluminum alloys were used in the experiment; the first is 1050-H24, which has a very low deformation resistance and thus achieved the best mechanical properties when friction stir welded using column shaped tool without threads as it produced welds with less defects than the other tools. The second one is 6061-T6 alloy which did not show any significant respond to changing the tool used in FSW in terms of microstructure and mechanical properties. It was noted that 6061-T6 alloy has a higher resistance to deformation but still considered relatively low. The third one is 5083-O alloy which has the highest deformation resistance among the three alloys. The mechanical and microstructure of the friction stir welded 5083-O were only affected by tool geometries at relatively high rotational speed. It was found that at a rotational speed of 1500 rpm, the triangular prism tool yielded the best weld; whereas, at a rotational speed of 800 rpm, the column with threads tool achieved the best weld and finally, at the lowest rotational speed of 600 rpm, the tool geometries did not have a significant effect on the mechanical properties and microstructure of the welded material.

An Evaluation of FSW of aluminum alloys AI-2219 and AI-2195 samples with different surface finish was done by Adapa et al. [16]. Four samples were made; the first sample with anodized joints yielded the worst results as it did not withstand half the load the other samples handled and achieved less than 1% elongation before fracturing. The other three samples with surface finishes were anodized root and crown surface, cleaned surface and natural oxide on surface; the three FSW samples endured almost the same amount of load before fracturing. Nonetheless, the sample

with anodized root and crown surface was considered the best as it achieved a 14% elongation compared to 5% and 7.2% for samples with cleaned surface and natural oxide on surface, respectively.

Khodir et al. [17] studied the effect of backing material on the thermal history, microstructure and hardness of aluminum alloy 2024-T3. The samples were all welded at a rotational speed and feed rates of 1250 rpm and 50 and 100 mm/min, respectively. Three types of backing materials were used in this study, SUS304 grade stainless steel, pure copper block and a combination of both. It was found that using stainless steel as the material of the backing plate resulted in the biggest grain size of 7.1 µm and 5.5 µm for 50 and 100 mm/s feed rates, respectively. While the smallest grain size was found when using pure copper block, which was 1.7 µm at 50 mm/s and 1.3 µm at 100 mm/s. In addition, it was noted that a higher peak temperature results in a higher hardness in the stir zone but a lower one in the heat affected zone which was found when using stainless steel backing plate. On the other hand, an increase in heating/cooling rate results in a higher hardness in the heat affected zone compared to the stir zone which is the case when using pure copper and a combination of copper and stainless steel. Furthermore, the highest tensile strength was found when using a combination of copper and stainless steel backing plate; the tensile strength achieved was 427 MPa which is 93.6% of that of the base material.

A study on the defects formed during friction stir welding was conducted by Kim et al. [18] and presented three types of defects. The first defects are due to excess heat input; defects usually appear at high rotational speed and low feed where a large mass flash is ejected outside the stir zone due to the softening of the material caused by the excess heat input. The second type of defects is due to insufficient heat input; a cavity or a groove-like defect appears on low rotational speed and high feed rate due to deficient heat input causing the material not to stir sufficiently. The last type of defects is caused by abnormal stirring; this type of defects happen at high rotational speed and high feed rate. The defect is caused to the temperature difference between the top and the bottom of the stir zone, where the top contacting the tool shoulder has high temperature relative to the bottom part of the stir zone which causes cavities to form. This type of defect slowly decreases as the downward force of the tool increases. In another study on the forming of defects in FSW, Leal and Loureiro [19] investigated the effect of welding speed on forming defects in different aluminum

alloys. In that study, 6063-T6 alloy was friction stir welded at a 500 mm/min and found to form fewer defects than 5083-O and 2024-T3 alloys which were welded at 150 to 600 mm/min and 200 to 400 mm/min, respectively. Nonetheless, 6063-T6 alloy FSW sample had a severe decrease in hardness in the weld; whereas, in the other two samples, 2024-T3 alloy FSW sample had a very small decrease in hardness, and the 5083-O alloy FSW sample had a slight increase in the hardness. It was found that an increase in the welding speed causes an increase in the rate of void formation; nonetheless, other factors may have an effect on void formation like the alloy used and the rotational speed as discussed earlier.

Cavaliere et al. [20] investigated FSW of dissimilar aluminum alloys 2024 and 7075. The tensile test done show that the weld achieved yield and tensile strengths are close to that of the weaker alloy with a very low elongation percentage compared to both alloys. It was also observed that the fracture occurred at the side of the weaker alloy. In addition, fatigue endurance curves were achieved in the study; it showed that FSW reduced the fatigue behavior of the material compared to the unprocessed material.

The effect of multi-passing in FSW and FSP was investigated in a limited number of studies [21-24]. Ma et al. [21] reported that both the ductility and strength are lower in the transitional zone between the welds in comparison to the weld nugget. It was also reported that following FSP passes achieved higher strength than preceding FSP passes. Additionally, multi-passes tend to have a slightly lower elongation than single pass FSP [22]. In terms of hardness, multi-passes do not have a significant effect as the hardness remains almost constant between passes [23].

A study of heat treatment effect on FSW welded alloys was conducted by Liu et al. [25] where 2219-T6 aluminum alloy was friction stir welded and tested by tensile testing. Post-weld heat treatment was found to have a positive effect on the tensile strength of the material as it increased from 81% to 89% of the tensile strength of the base material. Nonetheless, post-weld heat treatment caused the elongation of the FSW samples to decrease from 7.4% to 3.7%.

2.2 Submerged Friction Stir Welding

One of the applications of friction stir welding is that the ability of welding under water is more feasible than underwater arc welding [26]. Submerged friction stir welding uses the same tool and the same procedure used in air friction stir welding. However, for the same material, different weld parameters; for instance, feed rate and rotational speeds, must be used to obtain the same quality as in air friction stir welding.

Upadhyay and Reynolds [27] inspected the effect of thermal boundaries on friction stir welding. Friction stir welding was conducted on samples in air and samples submerged in water to determine what effect the quenching rates have on the joint properties and some of the weld response parameters. It was found that the peak temperature during the welding process was almost the same for the samples welded in air and those submerged in water; however, the cooling rate was higher for submerged samples than those welded in air. Additionally, submerged friction stir welded samples achieved a smaller grain size than the in air welded samples. This also indicates that the samples welded under water have a higher tensile strength than the samples welded in air, and this was proven experimentally. Nonetheless, it was observed that lowering the welding temperature by submerging the sample causes the sample to require more torque to stir the material; this resulted in the need of a higher rotational speed and thus required higher power consumption.

In addition, Zhang et al. [28] investigated the effects of rotation speed on submerged friction stir welding of aluminum alloys. The material used in the study is 2219-T6 aluminum alloy. The welding tool used had a shoulder diameter of 22.5 mm and a pin diameter and length of 7.4 mm. The results obtained by Zhang et al. show that the tensile strength of the weld increases as the rotation speed increases from 600 to 800 rpm; then, it stays constant as the rotational speed increases from 800 to 1200 rpm, and finally, it decreases sharply as the rotational speed reaches 1400 rpm with void defects appearing on the weld. The increase of rotational speed causes the material to become softer and thus more proper stirring occurs; this causes an increase in the tensile strength of the welded material. However, as the rotational speed increases further, excessive heat is exerted on the material causing defects to from, as discussed earlier [18,19].

In another study on submerged friction stir welding, Fu et al. [29] studied the effects of water temperature on the weld quality and properties. A 7050 aluminum alloy sample was used in the experiment where it was friction stir welded in air, and submerged in cold and hot water. The results indicate that the best welding medium is hot water where the ultimate tensile strength of the weld was 92% of that of the unprocessed material, and the ductility increased to 150% compared to the unprocessed sample. The ultimate tensile strength of the samples welded in cold water and in air dropped to approximately 85% and 75%, respectively, with respect to unprocessed sample; whereas, the ductility increased in air by 30% and in cold water by 25% compared to unprocessed sample. These results are in accordance with those of another study conducted by Liu et al. [30] which also confirms that submerged friction stir welding has a positive effect on tensile strength of the material compared to conventional friction stir welding.

A variation of FSW, a material refinement method called Friction Stir Processing (FSP), is used to achieve ultra-fine grain structure [31 – 33]. Nonetheless, there was the issue of grain growth due to the sample being exposed to high temperature during the process. Hofmann and Vacchio [34] used submerging as a technique to increase the cooling rate of the sample and decrease the time it is exposed to high temperature. The method proved to radically reduce the amount of conductive heat flow in the process. This decrease in conductive heat resulted in a reduction in the average grain size and made it possible to achieve a grain size as small as 200 nm or less.

In a previous study [7], FSP of magnesium alloy AZ31 was conducted in air and submerged in hot and cold water. It was noticed that when the samples are submerged, the peak temperature and time above a reference temperature decreased significantly compared to the sample processed in air. The sample submerged in cold water achieved the smallest average grain size of 13.3 μm compared to 15.9 μm and 18.9 μm in FSP samples done in hot water and air, respectively. Nonetheless, the sample processed in hot water achieved the highest ultimate tensile strength and elongation compared to the other two samples.

2.3 Aluminum Alloy 5083

Aluminum alloy 5083 is a marine grade alloy and it is a significant material in several marine applications. Generically, the best specifications of aluminum alloys are the low density and high strength to weight ratio. Aluminum alloy 5083 has a density of 2650 $\frac{kg}{m^3}$ which is close to one third the density of steel, copper and brass. The main alloying element of 5000 series aluminum alloy is magnesium, which plays a role in strengthening the alloy in addition to other elements; the chemical composition of aluminum alloy 5083 is shown in Table 2-1. With the given advantages, in addition to being corrosion resistant, using aluminum alloy, ship design will weight 50% less than similar steel designs [35]. Whereas, using aluminum alloy in ship construction, the weight reduction in the ship body results in achieving higher speed and less energy consumption. Moreover, welded aluminum alloy plates are used widely in manufacturing large tanks to transport liquefied gases. Last but not least, 5000 series aluminum alloys have the potential to be processed and enhanced to achieve better mechanical properties depending on their application [12]

Table 2-1 Chemical Composition of Aluminum Alloy 5083 [52]

Al	**Cr**	**Cu**	**Fe**	**Mg**
94.2-95.6%	0.05-0.25%	>0.1%	>0.4%	4-4.9%
Mn	Si	Ti	Zn	
0.4-1%	>0.4%	>0.15%	>0.25%	

2.4 Numerical Modeling

Various studies have been conducted on numerical modeling of friction stir welding. Different models were constructed to analyze, study and predict the effects of friction stir welding and friction stir processing. Numerical modeling can aid in fully understanding specific details in the process; for example, strain evolution and material flow. Moreover, by validating the numerical results with experimental results, the numerical model can be used to predict changes in the results due to variations in the input parameters which saves experimental time and cost. Studies prove that 2-dimentional modeling of FSW is possible [36-38] but is relatively limited compared to 3-dimentional models.

Buffa et al. successfully created a model using commercial finite element analysis software DEFORM-3D which can predict the temperature, strain, strain flow and forces from the weld parameters [39]. The tool is modeled as a rigid body while the work piece is modeled as a single block to avoid contact instabilities if a backing plate is introduced. It was found that decreasing the feed rate causes an increase in the maximum temperature of the weld nugget and an expansion in the heat affected zone. In addition, it was reported that the thermal profile along the weld line is symmetric as opposing to the material flow which was found to be asymmetric while both are controlled by the rotational speed and feed rate of the welding tool.

Hamilton et al. [40] proposed an energy based thermal model with Johnson-Cook's plasticity formulation to predict the thermal profile during the FSW process. As it accounted the heat generated due to plastic deformation and heat loss due conduction to the backing plate, the results came in good agreement with the experimental data. The model accurately predicted the heat generation and maximum weld temperature at relatively higher rotational speeds. A comparison between the temperature profiles with and without accounting for the heat generation due to the plastic deformation shows that the results are closer and more accurate to the experimental results when the heat due to plastic deformation is included. Nonetheless, the model under predicts the maximum weld temperature at the lower rotational speeds due to the conventional approach used to compute the plastic energy.

A thermo-mechanical model was developed by Zhang and Zhang [41] to predict the variations in thermal histories and material caused by various welding parameters in friction stir welding. ABAQUS/Explicit commercial finite element analysis software was used to generate the model. Arbitrary Lagrangian-Eulerian (ALE) formulation was used to avoid excessive element distortion in the mesh due to high plastic deformation. Additionally, to avoid element distortion, mass scaling of 10^7 was determined by comparing internal and kinetic energy. The model successfully foretold results that are equivalent to the experimental results; it was reported that as the rotational speed increases, the welding temperature increases. Increasing the rotational speed also leads to an increase in the power consumption and residual stresses on the sample.

Schmidt and Hattel [42] produced a thermomechanical model to investigate the conditions where a perfect weld can be achieved by FSW and no void is formulated. The model was made using the commercial software ABAQUS/Explicit with ALE formulation and remeshing option to avoid excessive distortion in the mesh due to high plastic deformation. It was found that heat generated in the process is due to plastic dissipation and frictional dissipation depending on the sticking and sliding conditions at the instant. The mesh quality in this work was reduced to compromise the simulation time which was said to reach 14 days for 10 seconds of simulation on a high speed computer.

Despite the fact that several researches were conducted on the topic, only a few of them were concerned with submerged FSW. The current study focuses on understanding the effect of submerging on FSW in addition to the effect of welding parameters, such as rotational speed and feed rate on submerged FSW. Furthermore, most of the numerical models reported in the literature were developed using Lagrangian part definition in ABAQUS which requires high computational cost. The model in this study is developed using Eulerian material definition which significantly reduces the computational time.

Chapter 3 : Experimental Work

3.1 Specimen Description

The specimens used in this study are made of marine grade aluminum alloy 5083; specifications and composition are discussed in section 2.3. The properties of aluminum alloy 5083 are shown in Table 3-1. The samples used are 130 mm in length, 60 mm in width and 4 mm thick. The specimens used are cut from 4 mm sheets; holes are drilled on the sides of the specimen to allow clamping it in the specially designed tank for submerged friction stir processing, experimental procedures are discussed in more details in section 3.3. Before testing the received material, samples are cut and prepared under the same conditions of the FSW samples to assure that only the effect of FSW is observed. Tiny slots for thermocouple placement are made 2 mm away from the stir zone and along the weld line.

Table 3-1 Properties of Aluminum alloy 5083 [52]

Density	**Ultimate tensile strength**	**Elastic modulus**	**Elongation**
2650 $\mathbf{kg/m^3}$	290-320 MPa	72 GPa	17 – 23%
Hardness, Vickers	**Melting temperature**	**Thermal conductivity**	**Thermal expansion**
75-95 HV	570 °C	121 W/m.K	25 x 10^{-6} /W

3.2 Tools and Equipment

A specially designed steel welding tool is used for in air FSW and submerged FSW. The tool used in this study has a 15 mm diameter featureless shoulder and a 4 mm long threaded pin with a diameter of 5 mm. In addition, a vertical Computer Numerical Control (CNC) machine is used to drive the welding tool. The setup used to hold the specimen was designed and built to allow a dynamometer to be placed below the holding fixture for future use. Moreover, the steel fixture is designed so that it clamps the two aluminum pieces to be welded together while restricting them from moving or rotating in any direction. Figure 3.1 shows the used fixture as well as the used samples before welding. For submerging purposes, a plastic container is designed, so that the work piece can be clamped in and can be fitted in the CNC

machine. The submerging container used is 30 cm in length, 15 cm in width and 10 cm in height. Furthermore, the submerging tank has a capacity of 4.5 L and can be used to submerge the sample with coolant or water at any temperature. Besides, three K-type thermocouples are placed parallel to the weld line to record the temperature during the process. All the thermocouples are placed at a thickness of 2.5 mm and 2 mm away from the stir zone as shown in Figure 3.2. The three thermocouples are placed so that one is close to where the weld starts, one is exactly in the middle of the weld line and one is close to where the weld ends. Figures 3.3 and 3.4 show the full setup used to conduct the experimental work. Moreover, to have a better view of the thermal distribution along the specimen, an Ulirvision TI-395 infrared camera is also used to capture images during the welding process. Furthermore, the power consumption of the CNC machine during the process is recorded using a PS3500 power data logger to establish a comparison in power consumption as the rotational speed and feed rate are changed.

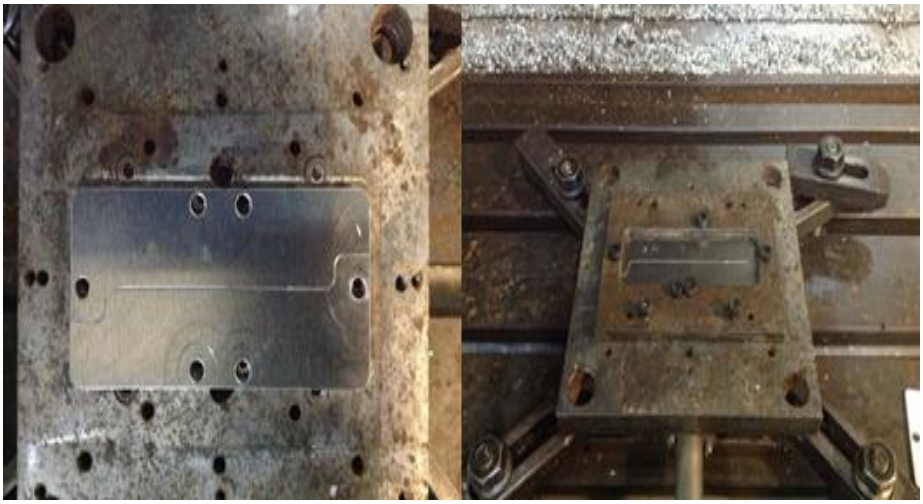

Figure 3.1 - Close up view of sample prior to welding and holding fixture

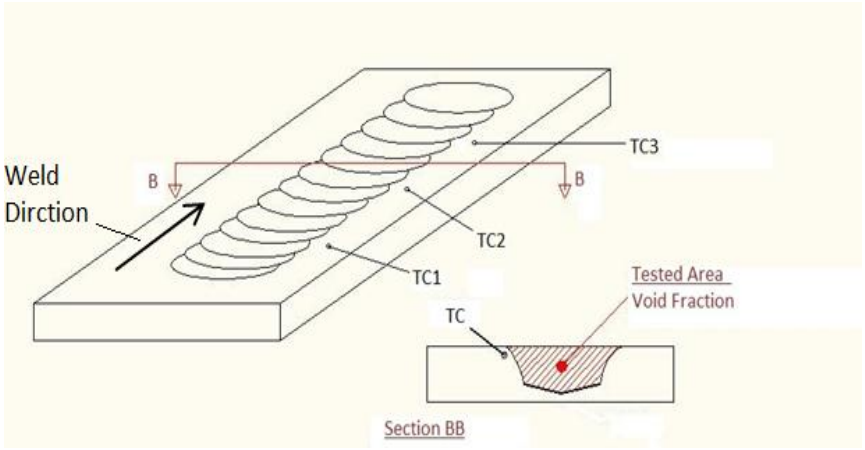

Figure 3.2 - Schematic diagram showing thermocouples locations and tested area

Figure 3.3 - Full set up used in experimental work

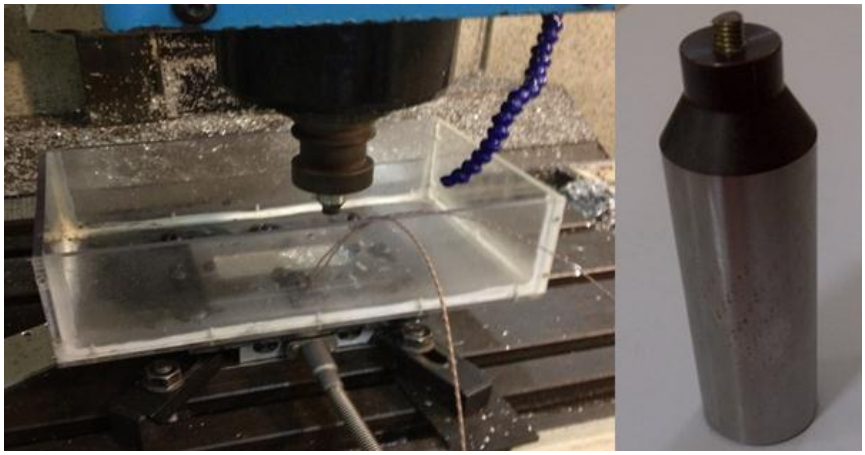

Figure 3.4 - Close view of experimental setup and welding tool

An Instron machine, shown in Figure 3.5, is used to conduct the tensile test to find the mechanical properties of the specimens. Moreover, an extensometer is used to find the elastic strain during the tensile test. The data found is used to plot a stress-strain curve to find various mechanical properties like the yield strength, tensile strength and ductility. The microhardness of submerged FSW samples is measured using a Qualitest microhardness testing machine, shown in Figure 3.6.

Figure 3.5 - Instron machine used for tensile testing

Figure 3.6 - Qualitest machine used for measuring the microhardness

3.3 Experimental Procedure and Process Parameters

The aluminum alloy 5083 sample is cut in two halves and clamped together in the specially designed plastic tank. The samples are plunged prior to the welding process as this decreases the heat input into the sample and thus results in better material properties [43]. The first set of in air FSW and submerged FSW samples are done at a rotational speed of 800, 1000 and 1200 rpm and a feed rate of 25, 75 and 100 mm/min. Another set of submerged FSW samples are done at higher rotational speed, between 1400 and 2000 rpm, as they require higher heat input to account for the heat lost in water due to its high heat capacity compared to air. All the conditions used in in-air FSW and submerged FSW are shown in Table 3-2. During in air FSW and submerged FSW, thermocouples are used to record the temperature of the sample along the weld line. The power consumption of the CNC machine during in air FSW and submerged FSW is recorded using the power data logger.

Table 3-2 Test matrix of input parameters where I means paramters used for in air FSW and S means parameters used for Submerged FSW

	800 rpm	**1000 rpm**	**1200 rpm**	**1400 rpm**	**1500 rpm**	**1700 rpm**	**2000 rpm**
25 mm/min	I / S	I / S	I / S	-	-	S	S
75 mm/min	I / S	I / S	I / S	S	S	S	S
100 mm/min	I / S	I / S	I / S	S	S	S	S

After in air FSW and submerged FSW are conducted, smaller specimens for tensile testing, microhardness measurement and void area fraction estimation are taken from the welded samples as shown in Figure 3.7. The tensile test is done at a rate of 2 mm/min with the extensometer measuring the elastic elongation until 0.6% elongation and then removed. The extensometer is removed as it could be damaged if the fracture occurs while it is still attached to the sample. Unlike the tensile test specimen, the microhardness and microscopic analysis specimen requires further preparation. All the specimens are ground with sand paper and then polished before being tested. Both the void area fraction and the average size are estimated manually. Finally, the microhardness is measured using a load of 1000 g and a dwell time of 10 s. It is measured in the stir zone as shown in the schematic in the previous sections. The average of 5 measurements on each sample is taken. More measurements along

the transverse and longitudinal direction of the weld are taken for one in air FSW and submerged FSW for further investigation on the microhardness profile in the stirred material and the heat affected zone.

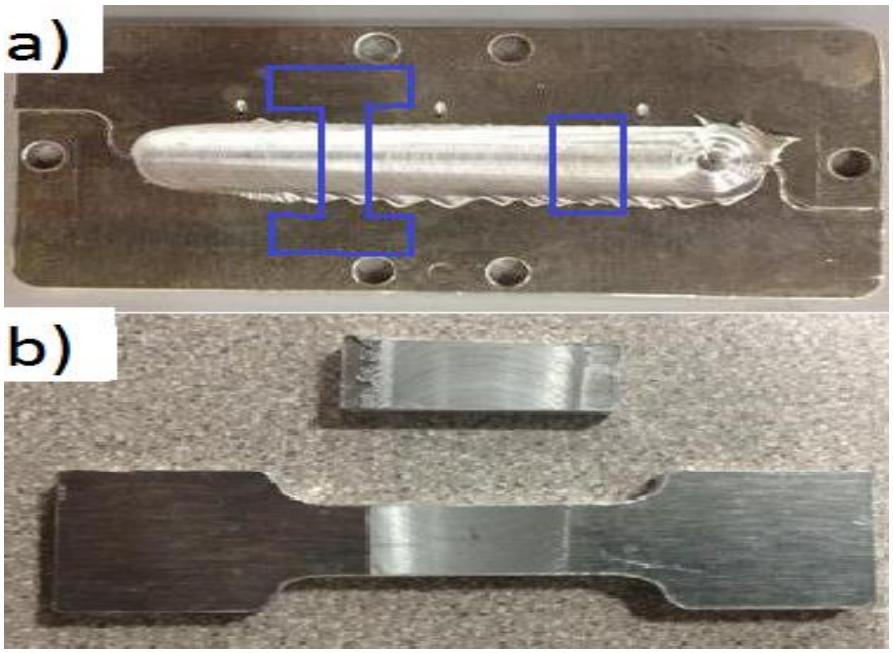

Figure 3.7 - (a) Welded sample (b) Specimens taken for tensile and microscopic testing

Chapter 4 : Results and Discussion

Both of the in air FSW and submerged FSW show very poor results at 800 rpm and at the three different feed rates. Void defects are created due to insufficient heating as reported in previous studies [18, 19]. At a low rotational speed, insufficient heat is generated which does not cause the material to soften enough to be stirred properly; therefore, create such defects as shown in the first samples in Figures 4.1 and 4.2. At 1000 rpm rotational speed, in air FSW attained defect free weld, but submerged FSW still created void defects along the line. As water has higher heat capacity than air, more heat is lost in submerged FSW than in in-air FSW causing it to still create void defects even when the rotational speed is slightly increased. As the rotational speed was increased to 1200 rpm, submerged FSW samples were still defective, as increasing the rotational speed did not increase the heat input sufficiently to stir the material properly. On the other hand, in air FSW samples at 1200 rpm attained defects due to excessive heat input as the overheated material splashed outside the stir zone. The rotational speed was only increased in submerged FSW, as in air FSW reached a rotational speed where proper stirring occurs and increasing it would only cause more defects to form. Increasing the rotational speed to 2000 rpm caused the void defects to eventually disappear leaving a good quality weld. The processing window for both in air and submerged FSW is summarized in Table 4-1.

Table 4-1 Processing window for in air and submerged FSW, where x denotes defected sample and O denotes defect free sample

	In air FSW			**Submerged FSW**						
	800 rpm	1000 rpm	1200 rpm	800 rpm	1000 rpm	1200 rpm	1400 rpm	1500 rpm	1700 rpm	2000 rpm
25 mm/min	x	x	O	x	x	x	-	-	X	x
75 mm/min	x	O	O	x	x	x	x	x	O	x
100 mm/min	x	O	O	x	x	x	x	O	O	O

Figure 4.1 – In air FSW samples at 75 mm/min and (a) 800 rpm, (b) 1000 rpm and (c) 1200 rpm

Figure 4.2 - Submerged FSW samples at 75 mm/min and (a) 1000 rpm, (b) 1500 rpm and (c) 1700 rpm

4.1 Effect of Submerging

As previously mentioned, water has a higher heat capacity than air which causes an increase in cooling rate and a decrease in peak temperature in submerged FSW compared to in air FSW. Limiting the heat input into the welded sample and increasing the cooling rate was proven to limit the grain growth in the welded sample, thus achieving better mechanical and microstructural properties [34, 43]. Figure 4.3 compares the temperatures recorded for the in air FSW and submerged FSW samples at constant rotational speed and feed rate. The graph shows the significant difference between the peak temperatures of the two samples. The thermocouple recording of the sample welded in air reached a peak temperature of 267 °C and stayed above 100 °C for more than 40 seconds. In contrast, the sample welded underwater reached only 82 °C and settled back to 40 °C in almost 10 seconds. Figure 4.4 compares the temperature recorded for two defect free in air FSW and submerged FSW samples at 1000 rpm and 1700 rpm, respectively. Even with the increase of rotational speed, the peak temperature difference between the two samples is still almost 100 °C, and the in air FSW sample took almost 20 more seconds to drop to less than 100 °C.

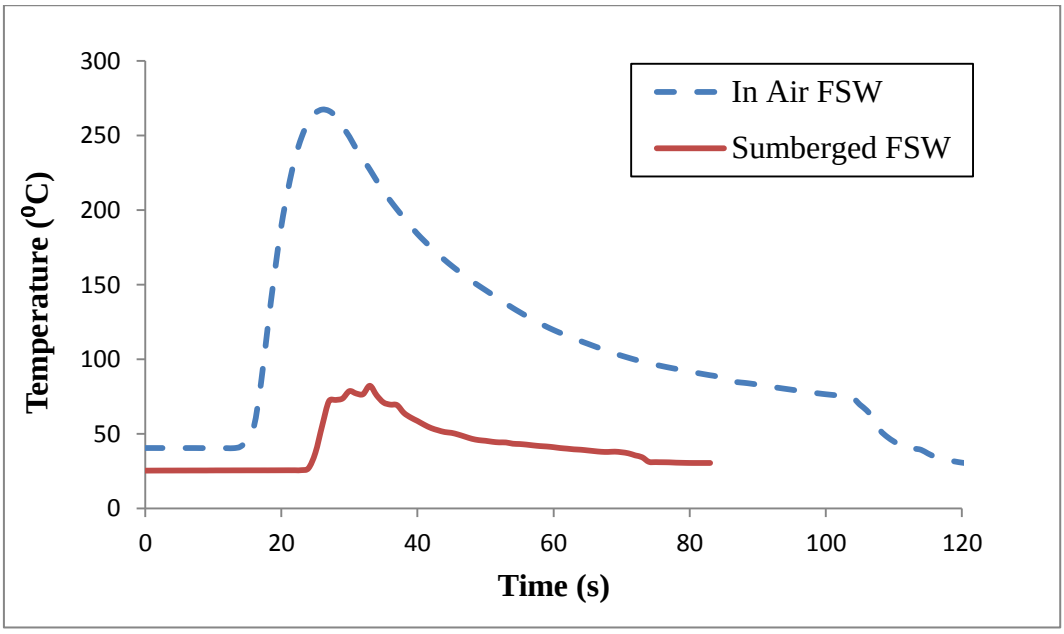

Figure 4.3 - Comparison of temperature recorded between in air FSW and submerged FSW at 1000 rpm and 75 mm/min

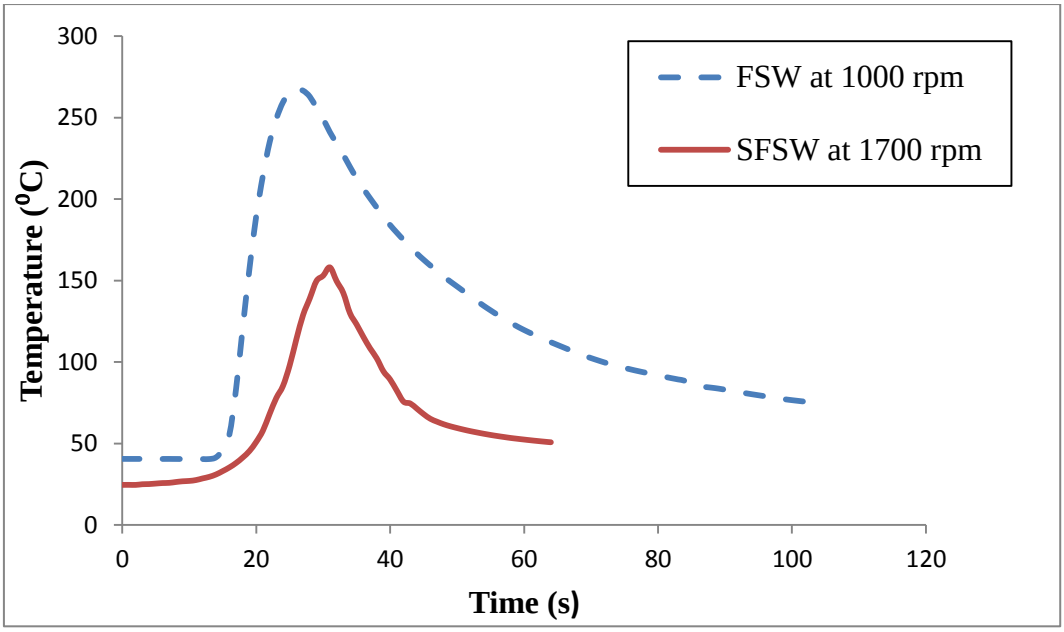

Figure 4.4 - Comparison of temperature recorded between in air FSW at 1000 rpm and 75 mm/min, and submerged FSW at 1700 rpm and 75 mm/min

One of the advantages of the in air FSW and submerged FSW is refining the microstructure [3, 4]. Microscopic images of parent material, in air FSW and submerged FSW are shown in Figure 4.5. The void area fraction and average void size are estimated; an image of 0.25 mm x 0.19 mm is used for the void area fraction estimation of each sample. The void area fraction estimated for the parent material was 4.1% with an average void size of 25.2 μm^2. In in-air FSW sample, at 75 mm/min and 1000 rpm, the void area fraction estimated was lower than the parent material at 3.2%, but the average void size was 38.5 μm^2 which is significantly higher than the parent material. All submerged FSW samples achieved lower void area fraction and average void size than the parent material and in air FSW sample. The lowest void area fraction estimated was 1.29% for the submerged FSW sample at 1700 rpm and 25 mm/min; whereas, the smallest average void size estimated was 5.7 μm^2 for the submerged FSW sample at 1500 rpm and 100 mm/min. It can also be noted that voids in the parent material and in air FSW were more ambiguous than those in submerged FSW samples, which seems more uniform. All the submerged FSW samples logged at least 60% less void area fraction than the parent material and 45% smaller average void size than the parent material. The microstructure plays an important role in affecting the tensile properties of the material; finer grain structure and lower void

area fraction result in better mechanical properties [48]. General studies on the effect of microscopic voids on the mechanical properties of different metals and composites proved that the increase of void area fraction corresponds to a decrease in the ultimate tensile strength and the yield strength [53, 54].

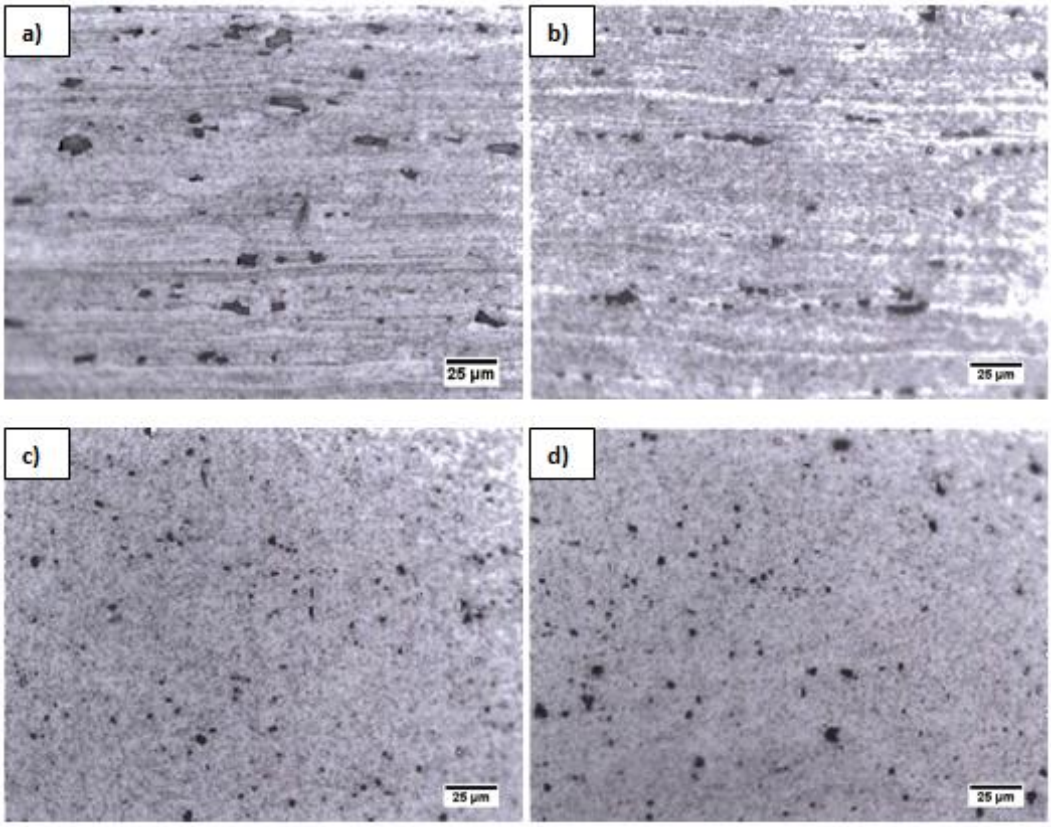

Figure 4.5 - Microscopic images of (a) Parent material (b) in air FSW sample at 1000 rpm and 75 mm/min (c) Submerged FSW at 1400 rpm and 100 mm/min (d) Submerged FSW sample at 1700 rpm and 75 mm/min

The microhardness profile of in air FSW and submerged FSW samples at the same rotational speed and feed rate can be viewed in Figure 4.6. The measurements were taken 2 mm from the top along the transverse direction of the weld where a measurement was taken every 0.5 mm. The results show that the microhardness values in the retreating side are slightly higher than the ones on the advancing side. The increase in microhardness in the retreating side is due to the lower heat input compared to the advancing side [7]. This phenomenon occurs as the rotation of the tool acts in the same direction of the weld in the advancing side while it acts in the opposite direction of the weld in the retreating side. The submerged FSW sample achieved higher microhardness values than the sample welded in air which is also due to the lower heat input in the submerged FSW than the in air FSW samples. The

highest microhardness value measured in the submerged FSW samples was 121.6 HV; whereas, in the in air FSW samples, its highest microhardness reading was 89.6 HV. The highest microhardness value recorded in all of the studied samples was the submerged FSW sample at 800 rpm and 25 mm/min, which was the sample with the lowest rotational speed and feed rate making it the sample with the lowest heat input among all the samples studied. The lower heat input into the sample limits the grain growth during the process and thus aids in the grain refinement. The smaller grain size achieved at lower temperatures results in an increase in the microhardness of the stirred material.

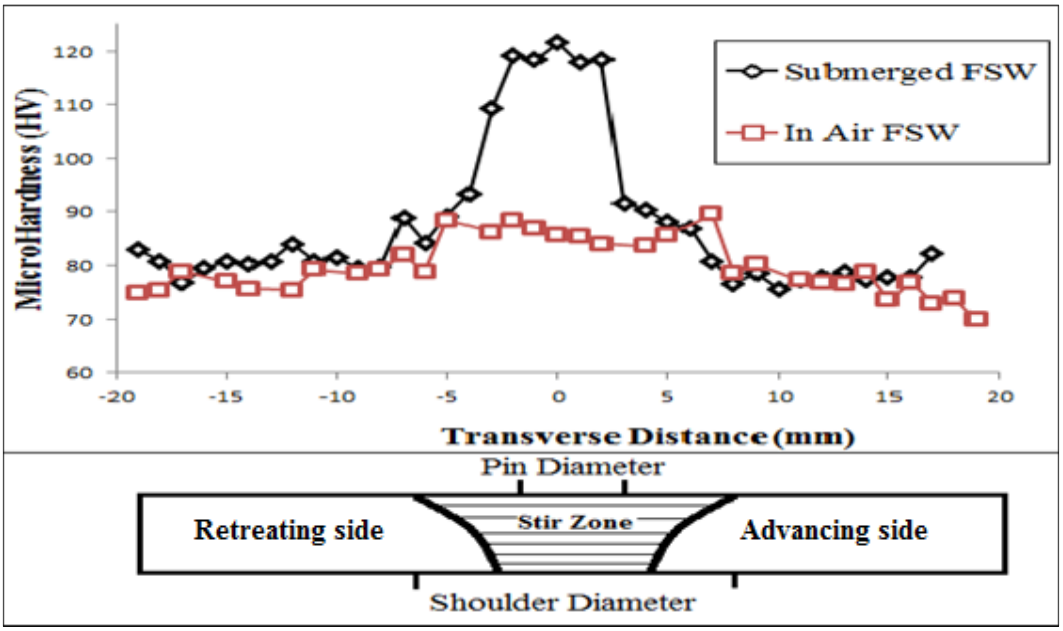

Figure 4.6 - Microhardness measurements on the transverse direction of the weld

The effect of submerging on the tensile properties could be predicted from the results previously presented in this chapter. The stress-strain curves of unprocessed parent material, in air FSW and submerged FSW at 1000 rpm and 75 mm/min are presented in Figure 4.7. From the results presented previously, at these conditions, the in air FSW sample achieved good quality defect free weld and the submerged FSW sample done was defective. As expected, the tensile test of the submerged FSW sample gave very poor results compared to the in air FSW and unprocessed material. The void defects on the sample caused it to fracture before even reaching 110 MPa and 10% elongation. The in air FSW sample fractured after reaching 236 MPa which is 79% of the ultimate tensile strength of the parent material which fractured at 302

MPa. Moreover, the in air FSW sample recorded a 66% increase in percent elongation compared to the parent material. Unlike the microhardness measurements, the tensile test is affected by the visible defects on the surface of the weld. Hence, even if the samples at the lower rotational speeds achieved finer microstructure, the visible void defects on the surface of the weld will cause the sample to fracture earlier in the tensile test and thus show poor tensile properties. In Figure 4.8, the comparison is between two defect free in air FSW and submerged FSW samples. The samples used in the comparison are an in air FSW sample at 1000 rpm and 100 mm/min and a submerged FSW sample at 1700 rpm and 75 mm/min. The submerged FSW sample had the upper hand in this comparison as it achieved the same tensile strength as the parent material in addition to 97.5% increase in percent elongation compared to parent material. Submerged FSW sample fractured after 31.6% elongation compared to 16% and 26% elongation for unprocessed material and in air FSW sample, respectively. The results are in accordance with previous studies done on the effect of submerging on tensile properties where sample welded underwater achieved higher tensile strength and percent elongation in some cases [29, 30]. The water in the submerged FSW causes an increase in cooling rate and a decrease in peak temperature due to its higher heat capacity compared to air. Lowering the heat input exerted into the sample limits the grain growth that occurs during the process which in turn leads to a finer microstructure and better tensile properties [27].

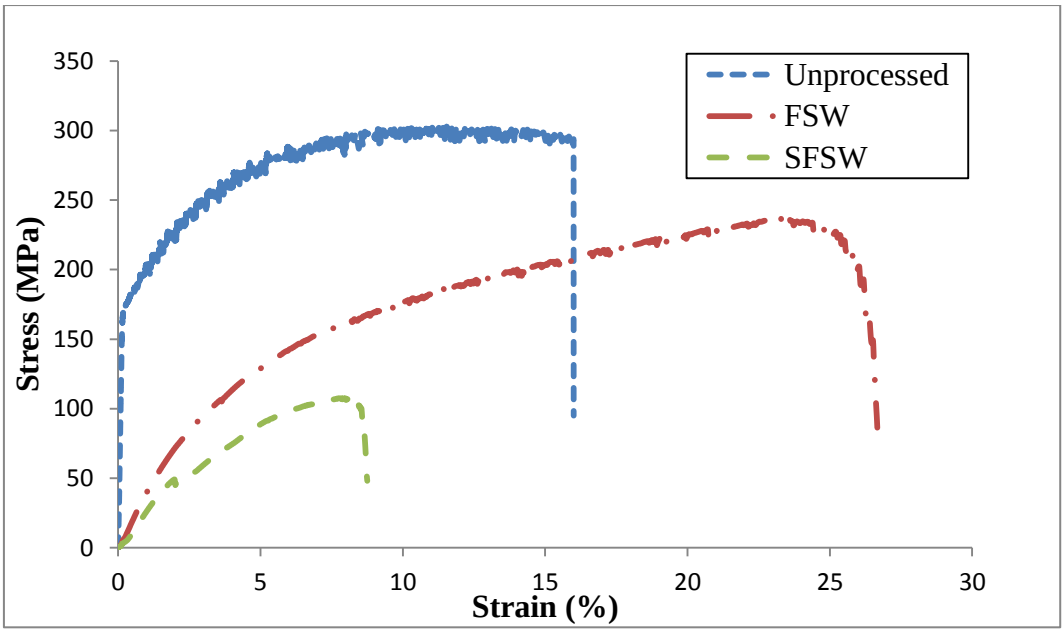

Figure 4.7 - Stress-strain curves of unprocessed samples, in air FSW and submerged FSW samples at 1000 rpm and 75 mm/min

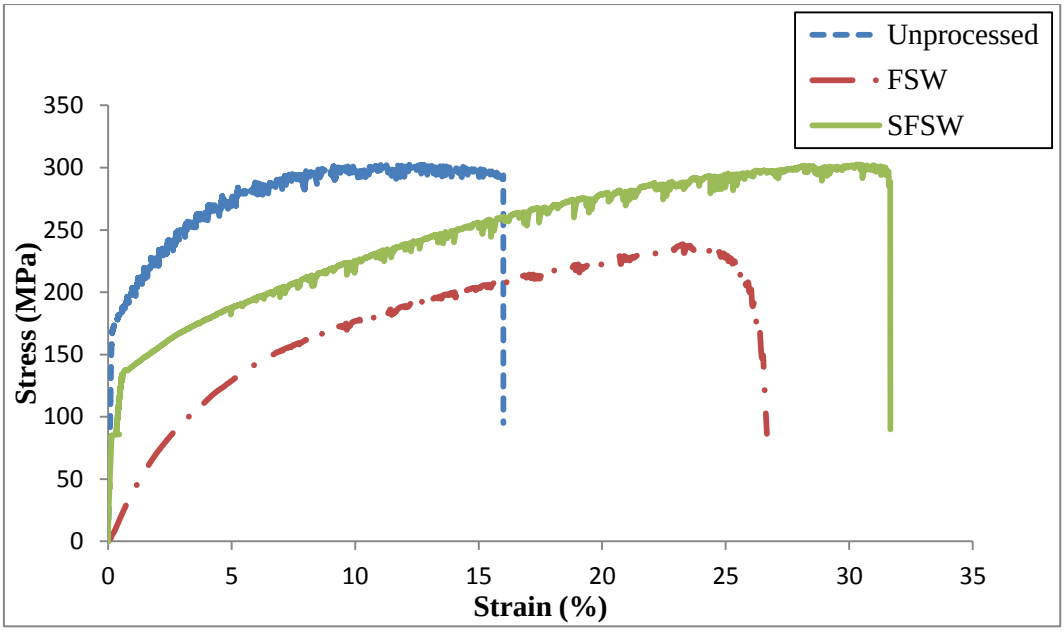

Figure 4.8 - Stress-strain curves of unprocessed material, in air FSW at 1000 rpm and 100 mm/min, and submerged FSW at 1700 rpm and 75 mm/min

The effect of submerging on power consumption can be viewed in Figure 4.9. The figure shows a slight decrease in power consumption in submerged FSW compared to in air FSW. Explanation for this phenomenon was not included in any previous research. Although a former study reported similar power consumption for both samples welded in air and underwater, in that case, it was for magnesium and at a considerable higher rotational speed [34]. Since both of the samples were welded at the same rotational speed and feed rate, the CNC machine should consume the same amount of power in both samples. The fact that it consumed less power in submerged FSW than in air FSW indicates that there is a factor assisting the CNC machine during submerged FSW. The justification for the decrease in power consumed could be because the water acts as a lubricant which reduces the friction between the tool and the sample and thus reduces the force required to drive the tool forward. The two samples compared were welded at 1000 rpm and 75 mm/min. As shown earlier in this chapter, the in air FSW sample at these welding conditions was defect free and the submerged FSW sample was defective. This could mean that the void defects appearing on the submerged FSW sample at relatively low rotational speed could be a result of lower friction force due to slip caused by water in addition to the heat lost to water.

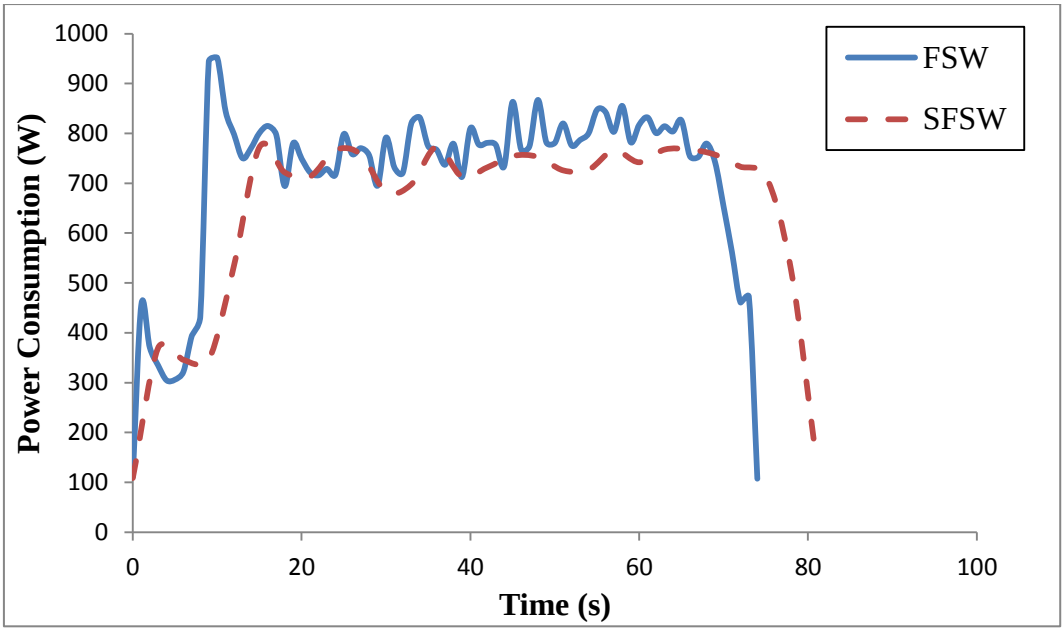

Figure 4.9 - Power consumed during in air FSW and submerged FSW at 1000 rpm and 75 mm/min

4.2 Effect of Rotational Speed

Figure 4.10 shows the effect of rotational speed on in air FSW. With raising the rotational speed from 800 to 1200 rpm, the friction heat input into the work piece increases causing the temperature to rise. The sample at 800 rpm and 75 mm/min reached a maximum temperature of 191 °C, while the samples at 1000 rpm and 1200 rpm reached a peak temperature of 267 °C and 406 °C, respectively. The increase in rotational speed did not have any direct impact on the cooling rate in the in air FSW samples. However, as the samples at higher rotational speed reach higher peak temperature, more time is required for them to cool down. Variation of rotational speed in submerged FSW had the same effect as in in-air FSW. The temperature increased as the rotational speed increased, as shown in Figure 4.11. Nonetheless, the peak temperature change between the different samples is lower than in air FSW. The lowest recorded peak temperature is 68 °C at 1000 rpm, while the highest recorded peak temperature is 158 °C at 1700 rpm. The difference between peak temperatures of the lowest and highest rotational speeds in submerged FSW is lower than 100 °C while in in-air FSW, it is above 200 °C despite that the rotational speed was increased from 800 to 1200 rpm in in-air FSW and from 1000 to 1700 rpm in submerged FSW. The results come in agreement with the previous section, and explanation of the

defects in some of the samples is shown in Figures 4.1 and 4.2. The samples at lower rotational speed that showed void defects recorded the lowest temperatures among all the in air FSW and submerged FSW samples. On the other hand, the in air FSW sample at 1200 rpm recorded the highest temperature among all the samples and had a defect due to excessive heating. The results also came in agreement with what was reported in previous studies on the in air FSW and submerged FSW [7, 27, 28].

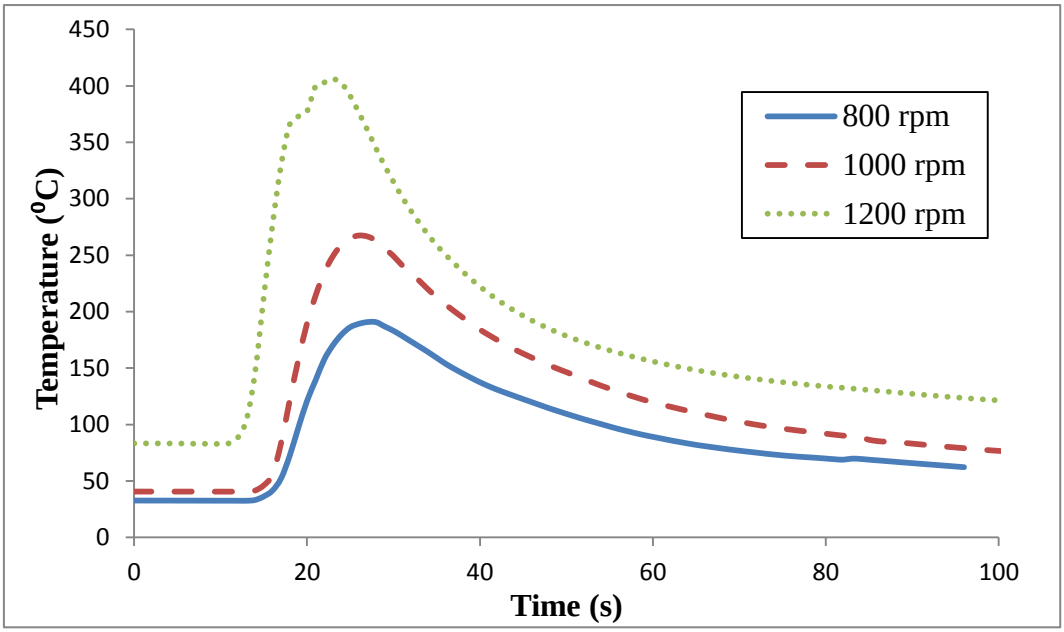

Figure 4.10 – In air FSW temperature recorded at constant feed rate 75 mm/min and three different rotational speeds

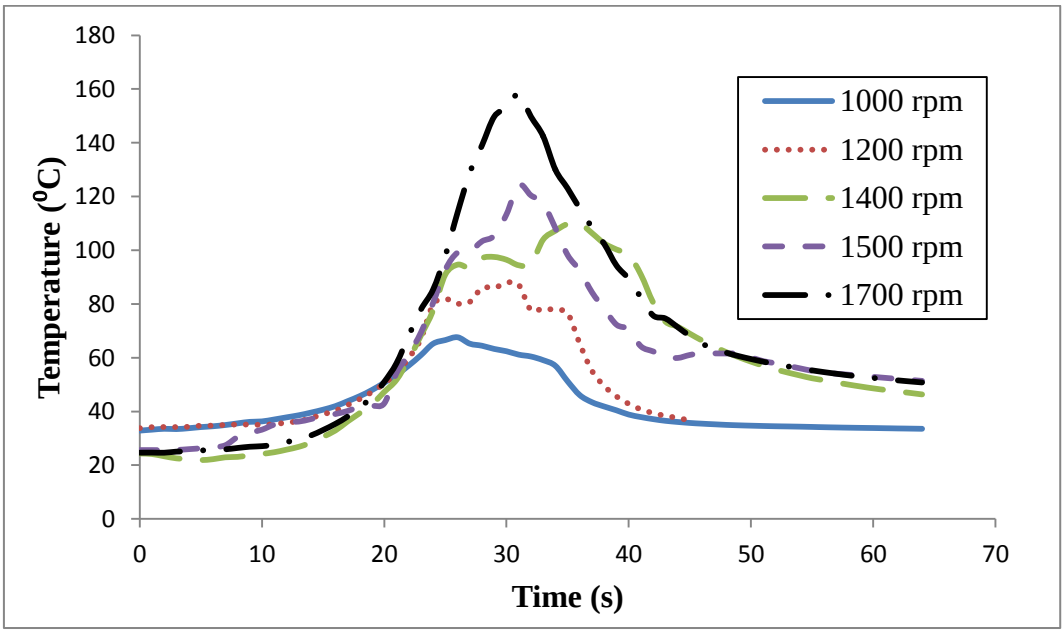

Figure 4.11 – Submerged FSW temperature recorded at constant feed rate 75 mm/min and different rotational speeds

The microhardness at different rotational speeds was measured and the results are shown in Figure 4.12. All the measurements were taken in the middle of the stir zone and 2 mm away from the top surface. The average of five readings are considered for each sample, refer to section 3.3 for more details about the measurement procedure. A decrease in microhardness occurred as the rotational speed increased. Even though the samples at lower rotational speed suffered from void defects, the microhardness was not affected by these defects as it was measured 2 mm below the surface of the weld. The decrease of microhardness was due to the increase in heat input as the rotational speed increased. Raising the rotational speed caused an increase in heat input that subsequently resulted in higher grain growth rates that affected the microhardness negatively [7, 46, 47]. In in-air FSW, the sample welded at 800 rpm achieved the highest microhardness of 95.3 HV; whereas, the lowest microhardness of 85.6 HV was measured in the sample welded at 1200 rpm. In submerged FSW, the lowest microhardness was 95.7 HV in the sample welded at the highest rotational speed of 2000 rpm, while the sample welded at the lowest rotational speed of 1200 rpm achieved the highest microhardness of 110.4 HV. On a positive note, only one sample achieved a lower microhardness than the base material and only by 0.1 HV; all the other samples attained higher microhardness than the base material.

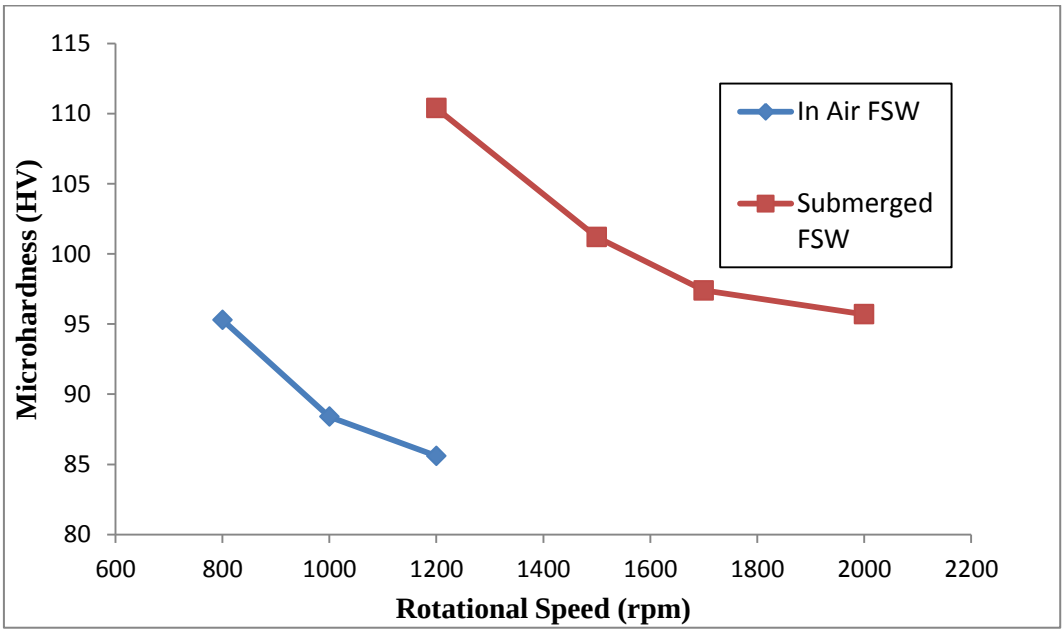

Figure 4.12 - Microhardness at 75 mm/min and different rotational speeds

The effect of rotational speed on tensile properties in in air FSW and submerged FSW can be viewed in Figures 4.13 and 4.14, respectively. In in-air FSW, the sample welded at 800 rpm was defective, as seen in the previous section, causing an unacceptable stress-strain curve. The sample barely reached one third of the tensile stress reached in the other samples and less than quarter the elongation reached by the other sample. At 1000 and 1200 rpm, the samples were proven defect free and appropriate stress-strain curves were obtained. Increasing the rotational speed from 800 rpm to 1000 rpm eliminated the voids in the sample and caused a drastic change in the stress-strain curve. The tensile strength at 1000 rpm reached 296 MPa and elongated by 32.6% before fracture. Moving from 1000 rpm to 1200 rpm, the changes were minimal in terms of yield strength and tensile strength; the only notable change was in terms of elongation as it increased from 32.6% in the 1000 rpm sample to 36.3% in the 1200 rpm sample. The same pattern can be noticed on submerged FSW samples; notable changes occurred on the stress-strain curves for samples between 1000 and 1500 rpm, and only slight differences occurred between 1500 and 1700 rpm. Previous studies reported that the tensile strength increases as the rotational speed increases up to a certain point and then experiments a drop as it increases further [28, 51]. The increase in rotational speed increases the heat input to the plate thus causes grain growth at higher rate. However, as the rotational speed increases from 800 to 1700 rpm, the temperature increases from an extent where it is insufficient to stir the material to an extent where it is enough for proper stirring. While increasing the temperature, proper stirring would still happen but with an increase in the heat input and thus inferior tensile properties. The results obtained from the tensile test do not come in agreement with the results found from microhardness test. As discussed earlier, the tensile test results are highly affected by defects appearing on the surface of the weld; whereas, microhardness and microscopic void results are affected by the resulting grain structure due to dynamic recrystallization and grain growth during the process.

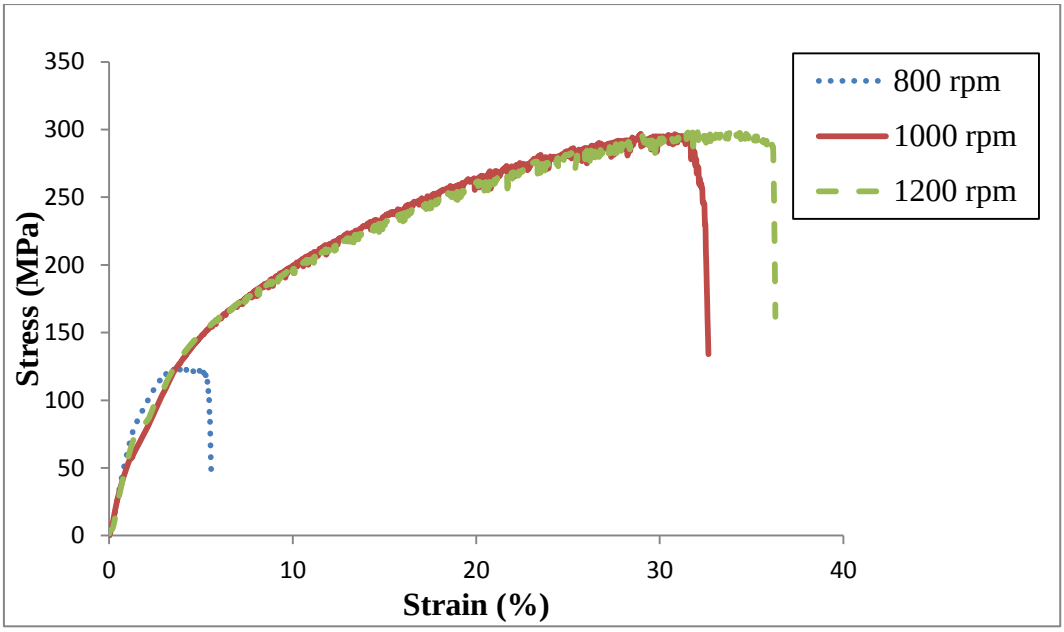

Figure 4.13 - Stress-strain curve of in air FSW samples at 100 mm/min and different rotational speeds

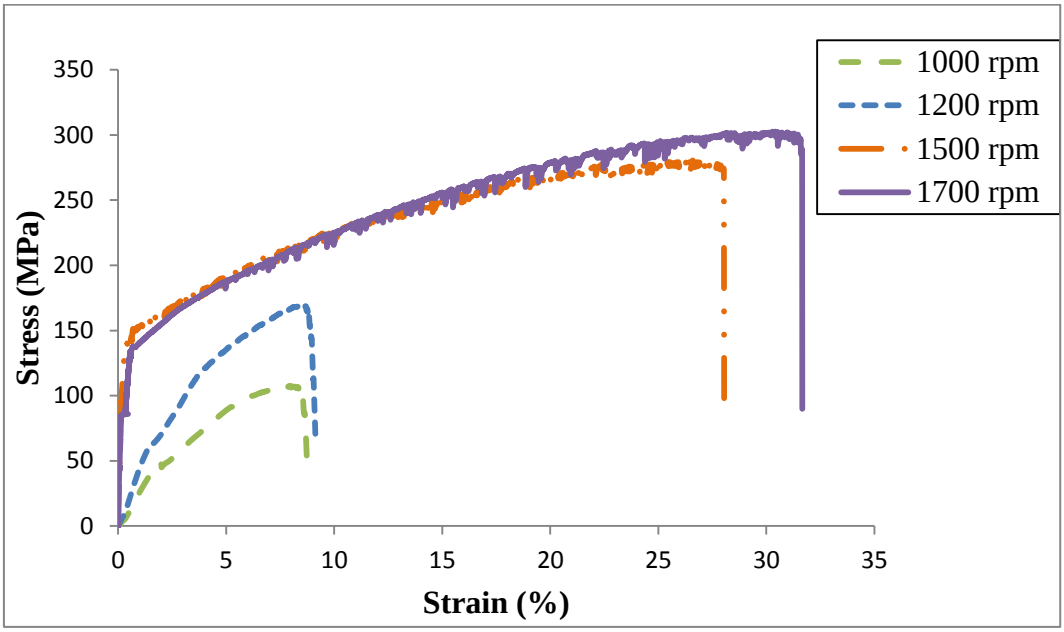

Figure 4.14 - Stress-strain curve of submerged FSW samples at 75 mm/min and different rotational speeds

The results on the effect of rotational speed on the in air FSW and submerged FSW came as expected. Figures 4.15 and 4.16 display the effect of rotational speed on power consumption in in-air FSW and submerged FSW, respectively. The power consumed during in air FSW and submerged FSW increased as the rotational speed increased. In in-air FSW, the average power consumption increased 677 W at 800 rpm to 851 W at 1000 rpm and finally to 872 W at 1200 rpm. It can be noticed that a noteworthy increase was recorded between 800 and 1000 rpm, and a minor increase

was recorded between 1000 and 1200 rpm. Relating the values to the weld quality discussed earlier in this chapter, at 800 rpm, the sample experienced improper stirring causing void defects to form which is not the case in the samples at 1000 and 1200 rpm. Hence, increasing the rotational speed from one that caused improper stirring such as 800 rpm to one that achieved smooth stirring such as 1000 rpm increases the power consumption significantly. In opposition, increasing the rotational speed from and to a value that achieved proper stirring does not cause a major increase in the power consumed. The same could be noticed for submerged FSW samples which suffered from improper stirring at 800, 1000, and 1200 rpm and achieved proper stirring at 1500 and 1700 rpm. The only notable change in power consumption was between the samples at 1200 and 1500 rpm, moving from defect infested weld to defect free weld.

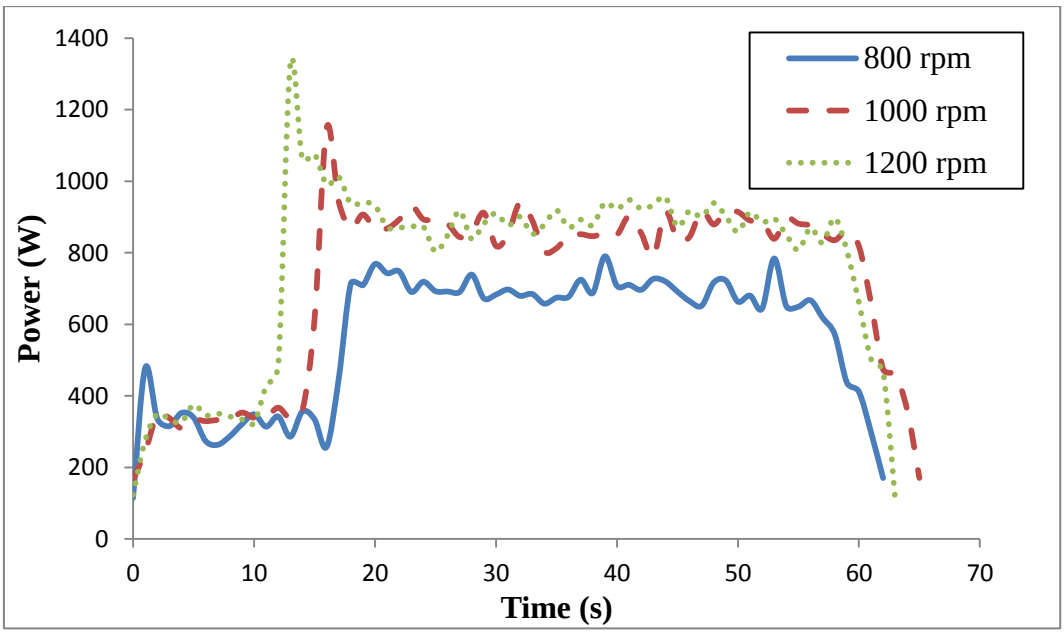

Figure 4.15 - Power consumption of in air FSW recorded at constant feed rate 75 mm/min and different rotational speeds

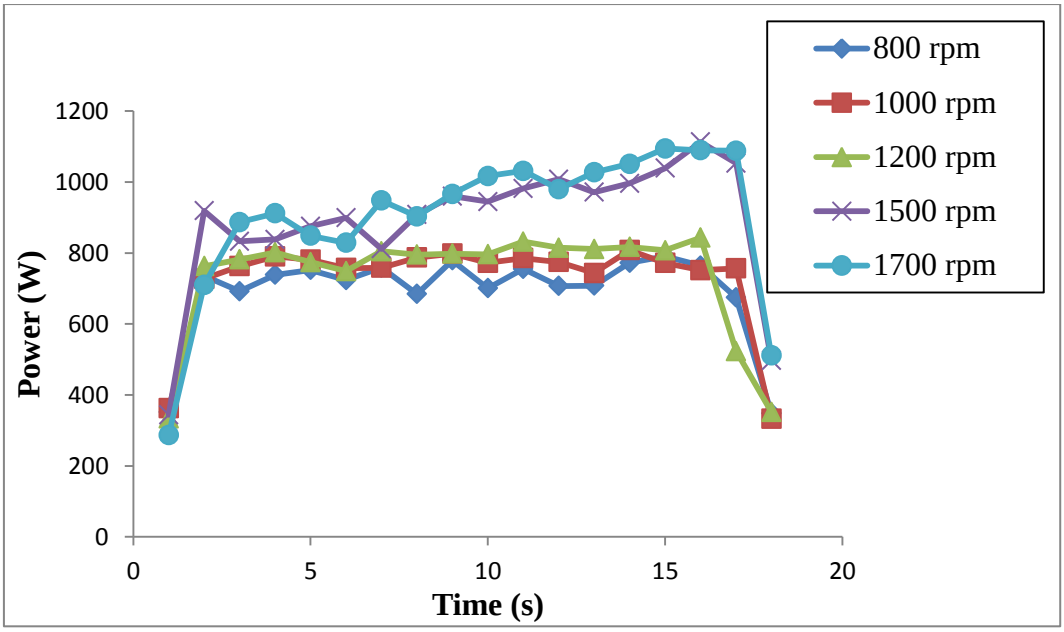

Figure 4.16 - Power consumption of submerged FSW recorded at constant feed rate 75 mm/min and different rotational speeds

4.3 Effect of Feed Rate

Temperature at constant rotational speed and various feed rates of in air FSW are shown in Figure 4.17. The change in feed rate did not have a big impact on the peak temperatures of the in air FSW samples. The three samples at 25, 75 and 100 mm/min were compared and their peak temperatures recorded were 298 °C, 287 °C and 279 °C, respectively. The bigger impact of changing the feed rates came in the time spent above a reference temperature. The sample welded at 25 mm/min remained above 100 °C for 216 seconds; whereas, the sample welded at 75 mm/min remained above 100 °C for 97 seconds, and finally, the sample welded at 100 mm/min remained above 100 °C for 44 seconds. The same was observed for the effect of feed rate on temperature in submerged FSW which is shown in Figure 4.18. The peak temperature at the lowest feed rate was the highest, and it decreased as the feed rate increased. At 25 mm/min, the maximum temperature reached was 110 °C, while at 75 mm/min and 100 mm/min, the peak temperatures were 99 °C and 85 °C, respectively. Similar results were obtained in previous studies; as the feed rate decreases, the time spent at a certain point increases, thus raising the temperature [46, 47]. Controlling the time of heat input into the sample can play an important role in affecting the mechanical and

microstructural properties as it can control the grain growth during the welding process.

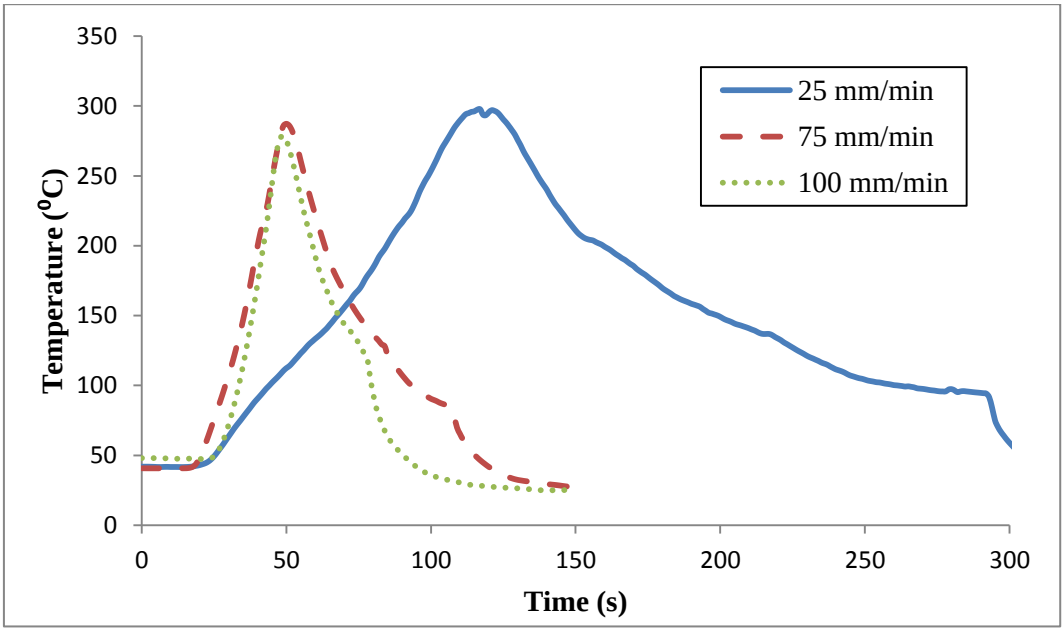

Figure 4.17 – In air FSW temperature recorded at constant rotational speed 1000 rpm and different feed rates

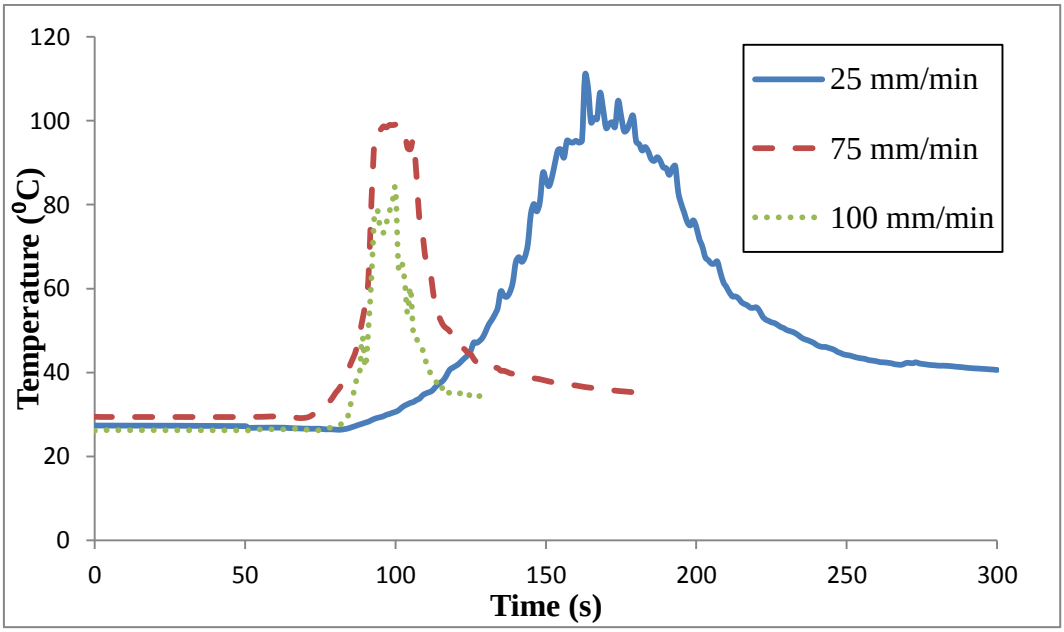

Figure 4.18 – Submerged FSW temperature recorded at constant rotational speed 1200 rpm and different feed rates

Similar to the effect of rotational speed, the feed rate is only effective in terms of heat input with neglecting any void formulated. Figure 4.19 shows the effect of feed rate on microhardness for in air FSW at 1000 rpm and submerged FSW at 1000 and 1700 rpm. In in-air FSW at 1000 rpm, the effect of feed rate was minimal; the

microhardness decreased from 89.5 HV to 86.4 HV as the feed rate increased from 25 mm/min to 75 mm/min and finally declined to 85.7 as the feed rate rose to 100 mm/min. The effect of feed rate became more notable in submerged FSW sample at 1000 rpm. The increase of feed rate from 25 to 75 mm/min reduced the microhardness from 124.3 HV to 118.7 HV; besides, raising the feed rate further to 100 mm/min caused a huge drop to 109.5 HV. Last but not least, the submerged FSW sample that was welded at 1700 rpm resulted in the most remarkable effect of feed rate. The microhardness dropped from 114.5 HV to 101.4 HV when the feed rate was raised from 25 mm/min to 75 mm/min, and then it decreased to as low as 93 HV as the feed rate increased to 100 mm/min. Although increasing the feed rate decreased the processing time and thus limited the grain growth, the microhardness dropped instead of increasing. A previous study by Sato et al. [50] state that the hardness could be highly affected by the precipitation distribution in the weld rather than the grain structure.

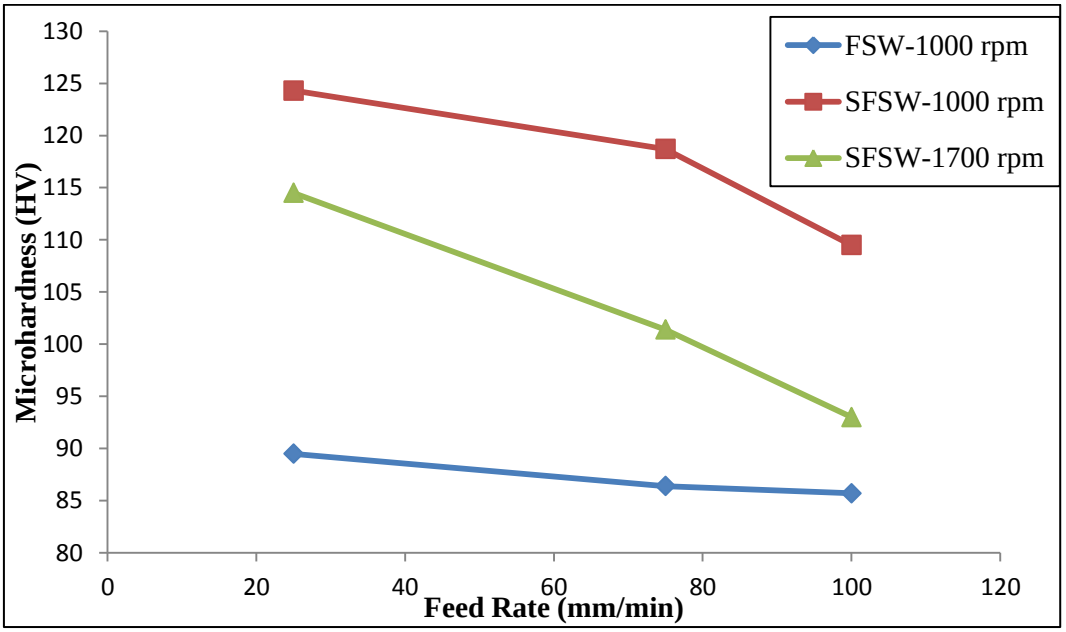

Figure 4.19 - Microhardness of in air FSW and submerged FSW at different feed rates

The effects of increasing the feed rate can be foretold from the temperature profiles. Since increasing the feed rate decreases the temperature, it also limits the grain growth during FSW and SFSW and consequently improves the tensile properties [19]. Figures 4.20 and 4.21 show the stress-strain curves at different feed rates for in air FSW and submerged FSW, respectively. In in-air FSW, the difference

in yield and tensile strength was insignificant. The only notable difference in in-air FSW samples was the increase in elongation at 100 mm/min which increased by approximately 6% compared to the other two samples. The dissimilarity in stress-strain curves is clearer for submerged FSW samples where variations in tensile strength, yield strength and elongation were recorded. The samples welded at 25 mm/min resulted in a very poor stress-strain curve where the tensile strength was almost 100 MPa lower than the other two samples, and the elongation was less than half the elongation of the other two samples. Comparing the samples welded at 75 mm/min and 100 mm/min, the sample welded at 75 mm/min reached higher yield strength than the sample welded at 100 mm/min. The difference in yield strength recorded was almost 43 MPa; the sample welded at 75 mm/min reached 172 MPa while the sample welded at 100 mm/min reached 129 MPa. Comparing the tensile strength, the sample welded at 100 mm/min reached higher tensile strength than the sample welded at 75 mm/min. The variation in tensile was only by 23 MPa as the sample welded at 100 mm/min fractured at 302 MPa, and the sample welded at 75 mm/min fractured at 179 MPa. The notable variance between the two samples was in elongation percentage; the sample welded at 100 mm/min reached 7% higher elongation compared to the sample welded at 75 mm/min. Overall, increasing the welding speed decreases the heat input into the sample, thus achieving better tensile properties [17] but can also result in abnormal stirring and formation of defects at very high feed rates [18, 19].

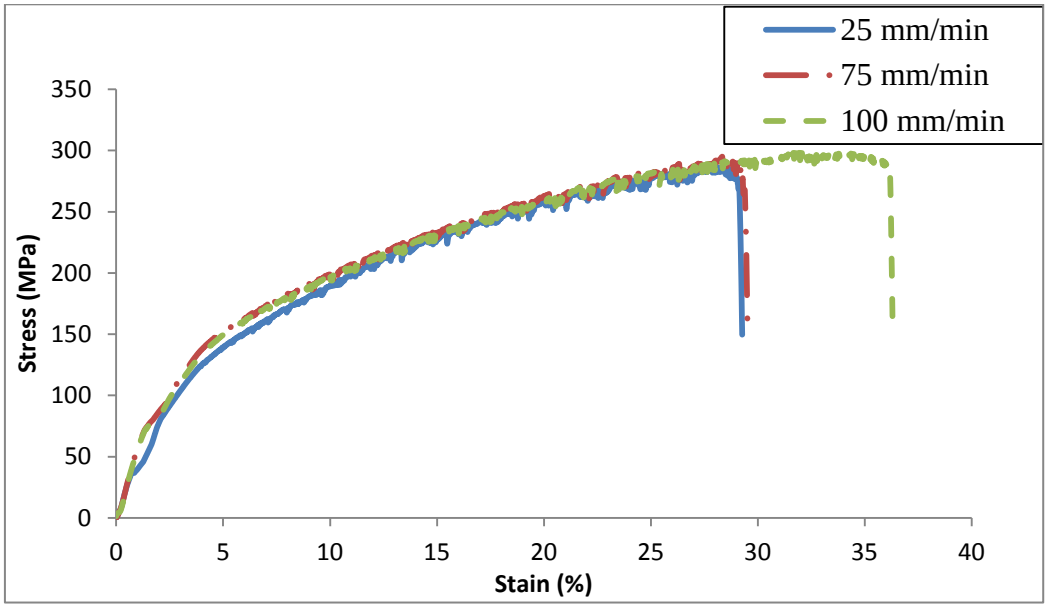

Figure 4.20 - Stress-strain curves of in air FSW samples at 1200 rpm and different feed rates

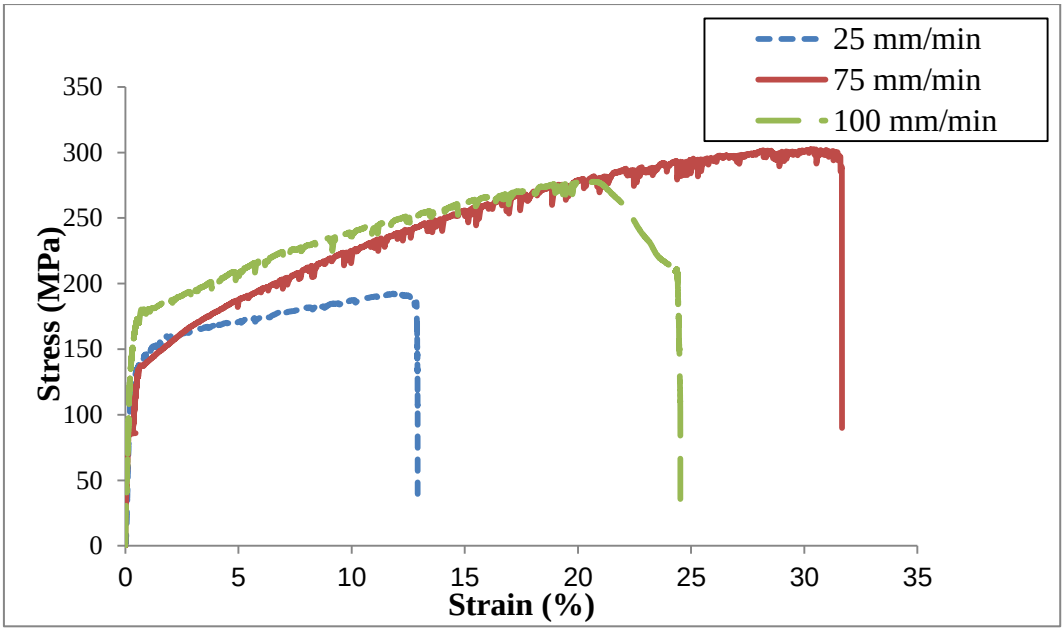

Figure 4.21 - Stress-strain curves of submerged FSW samples at 1700 rpm and different feed rate

Similar to the effect of rotational speed, the increase in feed rate caused a rise in the average power consumption in the in air FSW and submerged FSW. Nevertheless, the increase in average power consumption does not necessarily mean an increase in overall power consumed. In the previous section, all the samples had the same processing time because only the rotational speed was changed. In the case where the feed rate is changed, the processing time changes from one sample to another. Even though the sample at 25 mm/min had lower average power consumption than the sample at 75 mm/min, the processing time was longer for the samples at lower feed rate. Comparing the energy spent in W·h by multiplying the average power consumed by the processing time, the sample welded at 25 mm/min consumed 37 W·h; whereas, in air FSW at 75 mm/min consumed 14.6 W·h and finally, at 100 mm/min, the energy spent was 12.7 W·h. Thus, even though the increase in feed rate increased the average power consumption, the total energy consumed decreased due to the decrease in the processing time. Figures 5.26 and 5.27 are also in accordance with what is discussed in section 5.2.2 which is that the difference in power consumption between a defective sample and a defect free sample is higher than the difference between two defect free samples. In Figure 4.22, all the values where somewhat close as the three samples compared are defect free. On the other hand, in figure 4.23, the power readings of the defect free samples (75 mm/min and 100 mm/min) are close while the defective sample (25 mm/min) has significantly lower readings.

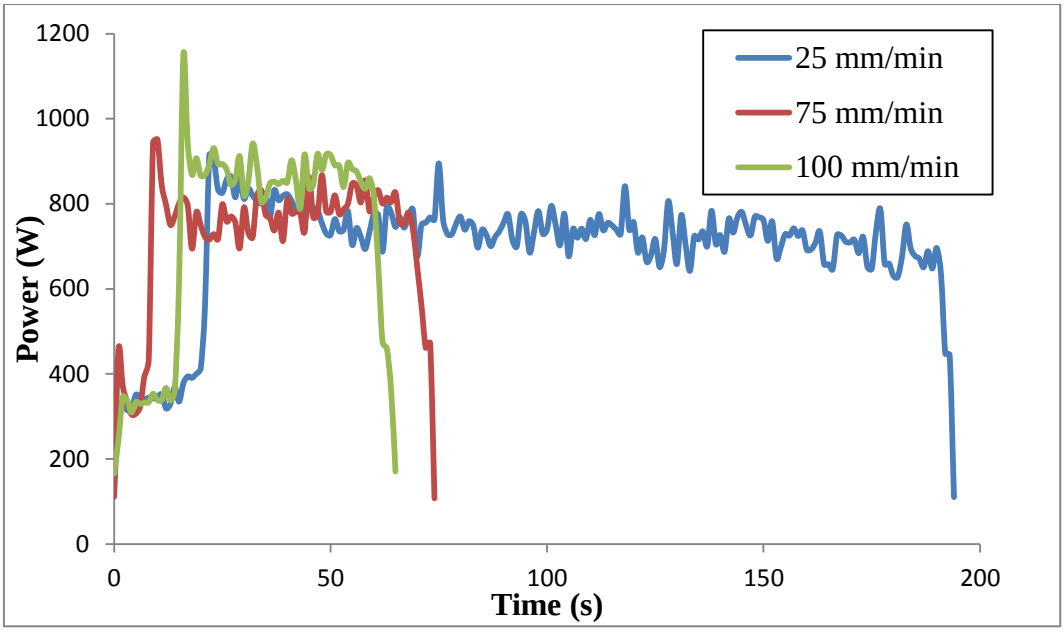

Figure 4.22 – In air FSW power consumption at constant rotational speed 1000 rpm and different feed rates

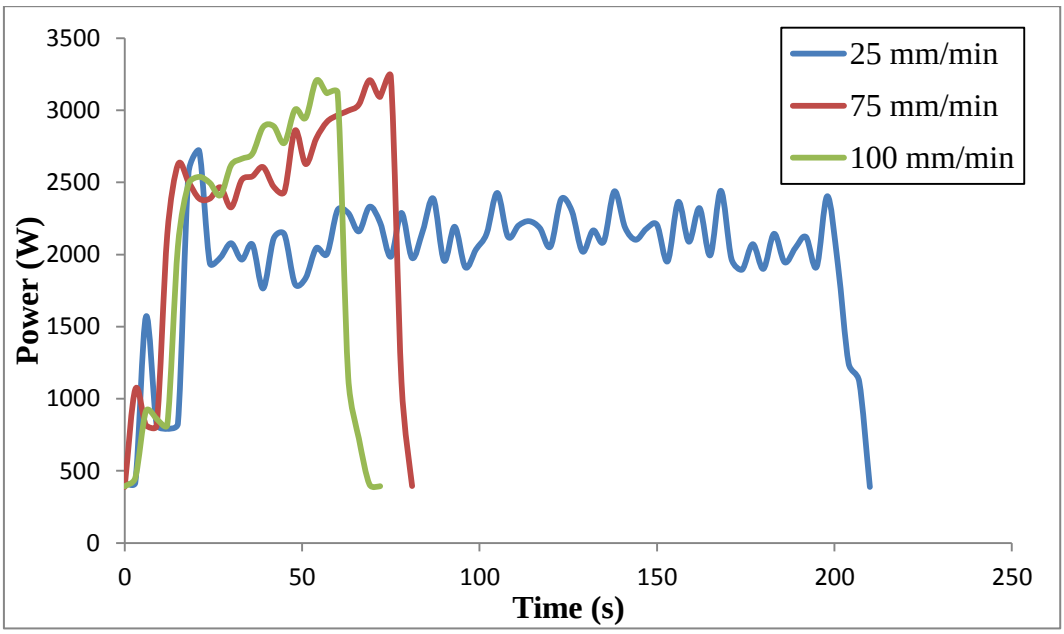

Figure 4.23 – Submerged FSW power consumption at constant rotational speed 1700 rpm and different feed rates

4.4 Microhardness Mapping

To have a better understanding of the effect of in air FSW and submerged FSW on microhardness, measurements were taken along the transverse, lateral and normal directions of the weld. The profile along the lateral and normal directions is discussed in this section, while the transverse direction was discussed in section 4.1. First, the microhardness of the base metal was measured at 5 different positions, and

the average taken was 85.7 HV. The microhardness profile along the normal axis of the weld can be seen in Figure 4.24. Moving closer to the top surface resulted in a decrease in microhardness as opposed to moving to the lower surface which increased the microhardness. The top surface is closer to the heat source which is the welding tool, while the lower surface loses heat to the backing plate. The increase in heat input causes more grain growth which in turn causes a decrease in the microhardness [49].

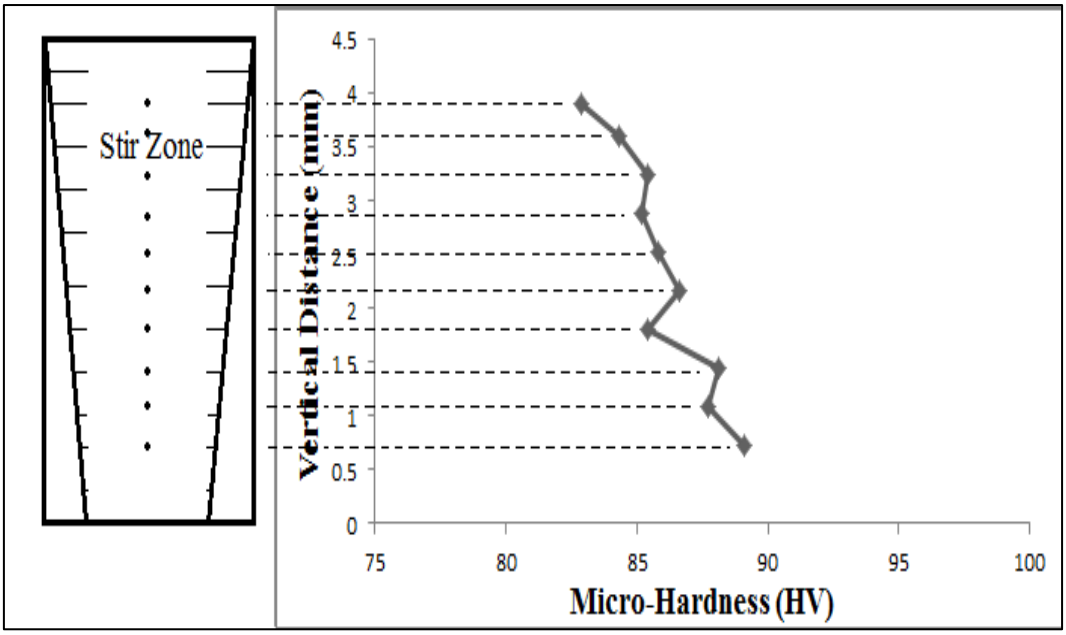

Figure 4.24 - Microhardness measurements along the lateral direction of the weld

The microhardness profile along the longitudinal direction of the weld is shown in Figure 4.26. The graph shows a decrease in microhardness at the end of the weld line compared to the beginning. Figure 4.25 shows the difference in three thermocouples readings on the in air FSW sample at 1000 rpm and 75 mm/min. The preceding thermocouple recorded lower peak temperature than the succeeding thermocouples. The first thermocouple recorded a peak temperature of 267 °C, while the second thermocouple recorded a peak temperature of 287 °C and finally, the third temperature recorded the highest peak temperature of 342 °C. The microhardness at the three different locations was 87.8 HV for the first one, 87.5 HV for the second one and 86.9 HV for the third one. The locations with the higher peak temperature achieved lower microhardness, as the temperature is the main cause of altering the microstructure and thus changing the microhardness [46, 47]. The increase in temperature recorded is due to the thermal conduction through the welded plate; by

the time the welding tool reaches the third thermocouple position, the temperature at that point will be increased to around half its peak temperature.

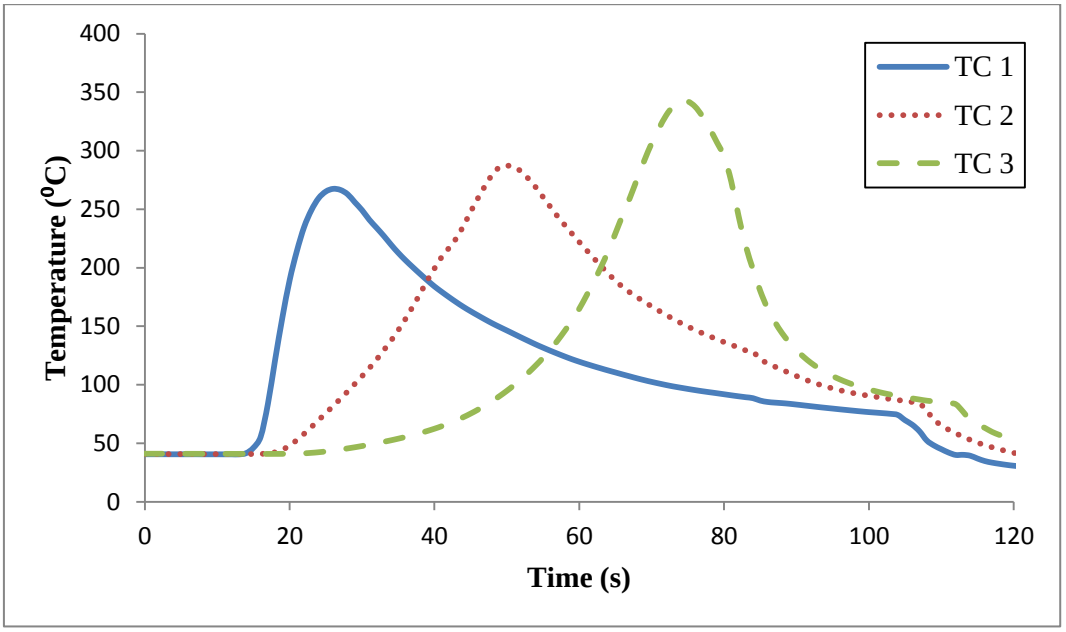

Figure 4.25 - Temperature recorded by three different thermocouples at different locations on in air FSW plate at 1000 rpm and 75 mm/min

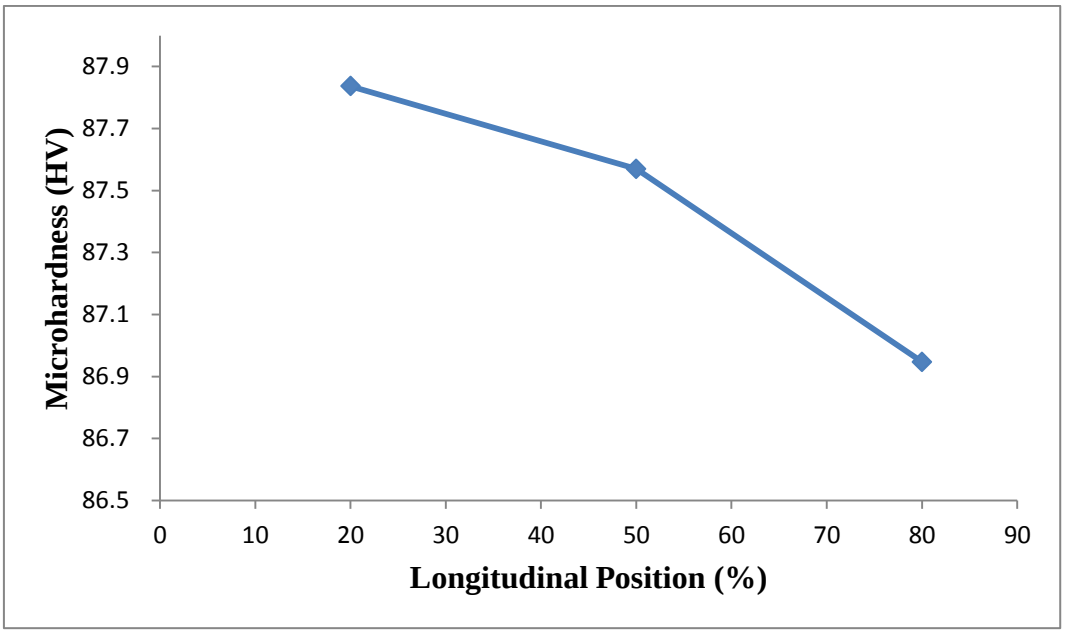

Figure 4.26 - Microhardness measurements on the longitudinal direction of the weld

4.5 Summary of Results

For convenience, the tensile properties and microscopic analyses of in air and submerged FSW are summarized in Figure 4.27 and Table 4-2, respectively. The results show a notable difference in the mechanical properties between in air FSW and submerged FSW at the same rotational speed and feed rate. The change in welding medium from air to water increases the amount of heat input required to achieve proper stirring. Nonetheless, it was noticed that the in air FSW and the submerged FSW samples achieved very close tensile strength at different rotational speeds and feed rates. The in air FSW sample welded at 1200 rpm and 100 mm/min attained very close results to the submerged FSW sample at 1700 rpm and 75 mm/min. This highlights the importance of controlling the heat input in FSW and its effect on the resulting properties. Moreover, the correspondence in results between an in air FSW and submerged FSW samples can simplify the finite element analysis of the process as the effect of water could be avoided.

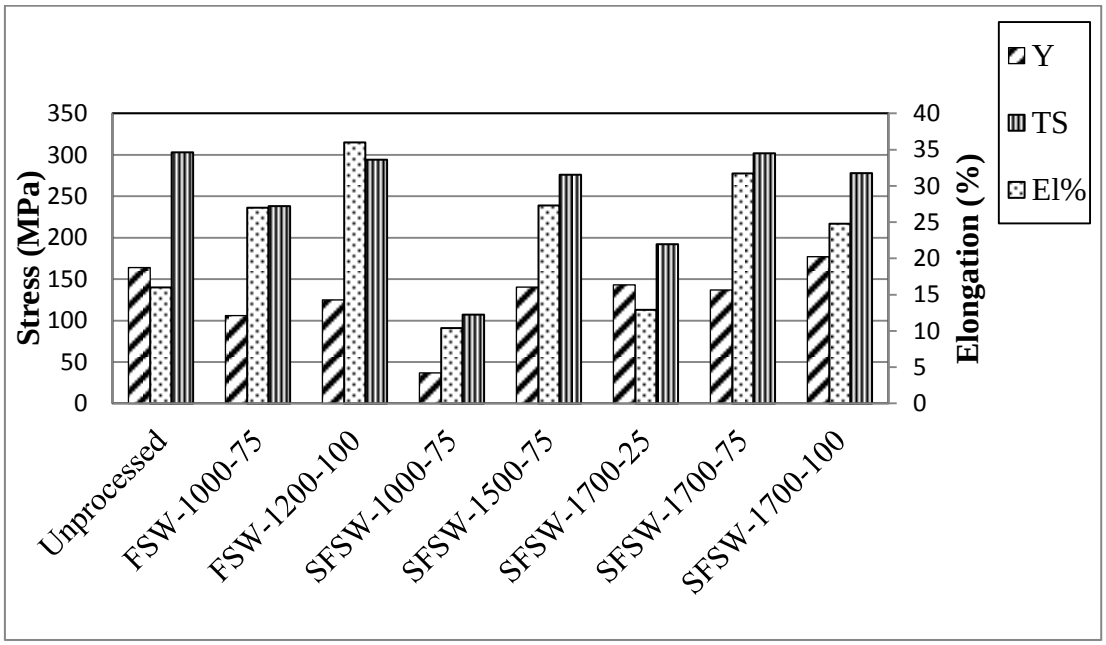

Figure 4.27 - Tensile properties of unprocessed material, in air FSW and submerged FSW samples at different conditions

Table 4-2 - Number of voids, void area fraction and average void area for selected samples

Sample	Number of voids	Void area fraction (%)	Average void area (μm^2)
In Air-1000-75	39	3.16	38.5
Submerged-1200-25	99	1.70	8.1
Submerged-1200-75	90	1.60	8.4
Submerged-1200-100	103	2.21	10.1
Submerged-1400-100	126	1.57	5.9
Submerged-1500-100	149	1.78	5.7
Submerged-1700-25	78	1.29	7.9
Submerged-1700-75	123	2.27	8.8
Submerged-1700-100	106	1.77	7.9
Submerged-2000-100	106	2.40	10.8
unprocessed	77	4.09	25.2

Chapter 5 : Finite Element Analysis

In this research, finite element (FE) simulation of friction stir welding is conducted using the commercial software ABAQUS. The aim of the present finite element modeling is to have a better understanding of the process with more detailed analysis than that of the experimental work. In addition, the finite element model is used to predict changes in the welding parameters to minimize the experimental work required. For the sake of simplifications, the FE model is based on friction stir processing (FSP) rather than welding. The two mechanisms are similar except that in friction stir processing, the aluminum plate is not cut into two pieces and then welded together; however, the material in the middle of the plate is just stirred instead.

5.1 Governing equations

The present FE model should account for two types of heat generation during the FSP process, heat generation due to plastic deformation, r^{pl}, and heat generation due to friction, q. To measure the heat generated due to friction, ABAQUS/Explicit [44] uses the following equation for the heat flux density:

$$q = q_k + q_r - f q_g \quad , \tag{5.1}$$

where q_k is the heat flux due to conduction, q_r is the heat flux due to radiation, f is the fraction of heat generated into the surface and q_g is the heat flux produced by the interface element due to frictional heat generation. The heat flux due to friction is defined as follows:

$$q_k = k\Delta T \ , \tag{5.2}$$

in which k is the heat transfer coefficient and ΔT is the temperature difference between the two surfaces. The heat transfer coefficient is dependent on the contact pressure, over-closure and the average temperature at the contact point.

The heat flux due to radiation is found by the following relation:

$$q_r = F[(T_1 - T^Z)^4 - (T_2 - T^Z)^4] \ , \tag{5.3}$$

where F is the gap radiation constant, T^Z is the absolute zero on the temperature scale used and T_1 and T_2 are the temperatures on surfaces 1 and 2, respectively.

Finally, the heat flux due to frictional heat generation is given as follows:

$$q_g = \eta\tau\frac{\Delta s}{\Delta t}, \tag{5.4}$$

where η is the heat fraction, τ is the frictional stress, Δs is the incremental slip and Δt is the time step. ABAQUS/Explicit applies the Galerkin method to solve the set of equation for finding the total heat generated due to friction.

As for the heat generation due to plastic deformation, ABAQUS/Explicit assumes that the plastic work caused by the accumulation of plastic strains converts into heat which, in turn, increases the heat flux per unit volume, r^{pl}, as follows:

$$r^{pl} = \beta\boldsymbol{\sigma} : \dot{\boldsymbol{\varepsilon}}^{pl}, \tag{5.5}$$

where β is the inelastic heat fraction which represent the percentage of the plastic work that is converted into heat inside the material, $\boldsymbol{\sigma}$ is the stress tensor and $\dot{\boldsymbol{\varepsilon}}^{\boldsymbol{pl}}$ is the plastic strain increment tensor. The notation ":" is the double dot product of the two matrices which results in a scalar. The inelastic heat fraction is considered a constant throughout the analysis. The plastic strain rate is defined for plasticity models as:

$$\dot{\boldsymbol{\varepsilon}}^{pl} = \dot{\varepsilon}^{pl}\boldsymbol{n}, \tag{5.6}$$

where $\dot{\varepsilon}^{pl}$ is the equivalent plastic strain rate and $\boldsymbol{n}$ is the flow direction which is a function of stress, plastic strain and temperature. Newton-Raphson technique is utilized to solve non-linear equations using the Backward Euler scheme as an integration tool. The dynamic flow stress of the material as well as the damage evolution throughout the plastic deformation is predicted using the Johnson-Cook (JC) plasticity and dynamic failure models that are already implemented in ABAQUS/Explicit.

The JC dynamic flow stress is given by the following relation:

$$\sigma = [A + B(\bar{\varepsilon}^{pl})^n]\left[1 + Cln\left(\frac{\dot{\bar{\varepsilon}}^{pl}}{\dot{\varepsilon}_o}\right)\right](1 - \left(\frac{T - T_{ref}}{T_m - T_{ref}}\right)^m), \tag{5.7}$$

where A is the static yield strength, B is the strain hardening coefficient, $\bar{\varepsilon}^{pl}$ is the equivalent plastic strain, n is the strain hardening exponent, C is the strain rate sensitivity factor, $\dot{\bar{\varepsilon}}^{pl}$ is the equivalent plastic strain rate, $\dot{\varepsilon}_o$ is the reference strain rate, T is the temperature, T_{ref} is the reference room temperature, $T_m$is the melting temperature and m is the thermal sensitivity parameter. On the other hand, the

damage evolution, ω, due to the accumulation of plastic strains inside the alloys is obtained using the following equation:

$$\omega = \sum(\frac{\Delta\bar{\varepsilon}^{pl}}{\bar{\varepsilon}_f^{pl}}) \,, \tag{5.8}$$

where $\bar{\varepsilon}_f^{pl}$ is the plastic strain at failure defined as follows:

$$\bar{\varepsilon}_f^{pl} = [d_1 + d_2 \exp\left(d_3 \frac{p}{q}\right)] \left[1 + d_4 \left(\frac{\dot{\bar{\varepsilon}}^{pl}}{\dot{\varepsilon_o}}\right)\right] \left[1 + d_5 \left(\frac{T - T_{ref}}{T_m - T_{ref}}\right)\right], \tag{5.9}$$

where $d_1$to $d_5$are the failure parameters, p is the hydrostatic pressure and q is the Von Misses stress.

5.2 FE Modeling

Finite element modeling of the friction stir welding process is a very complicated procedure as it involves excessive deformation accompanied with large amount of plastic straining and heat. Several attempts were made in this research to simulate the FSW process efficiently and also to accurately predict the temperature evolution throughout the deformation. The first FE model was generated using Lagrangian formulation for all of the three parts involved in the process; the tool, the aluminum plate and the backing plate. Both the tool and the backing plate were modeled as rigid bodies. The aluminum plate was merged with the backing plate. The tool was self-rotated, and the backing plate was modeled as a movable part to translate the welding plate in the welding direction. The plate was partitioned to refine the mesh of the stir zone in order to reduce the computational time. Tetrahedral 4-nod solid elements were utilized to model the large plastic deformation in the partitioned middle piece as shown in Figure 5.1; the rest of the plate; on the other hand, is modeled using 8-node linear brick elements. For such a model with a relatively high plastic deformation, a very fine mesh is required to avoid element distortion during the process. The very fine meshes as well as the high frequency remeshing technique used in the first model caused a drastic increase in the computational time. Attempt runs of this model on a high speed computer lasted for a very long period of time and didn't manage to model the first second of the process. With such an unrealistic computational time, the model was discarded even though it didn't experience any errors or crashes.

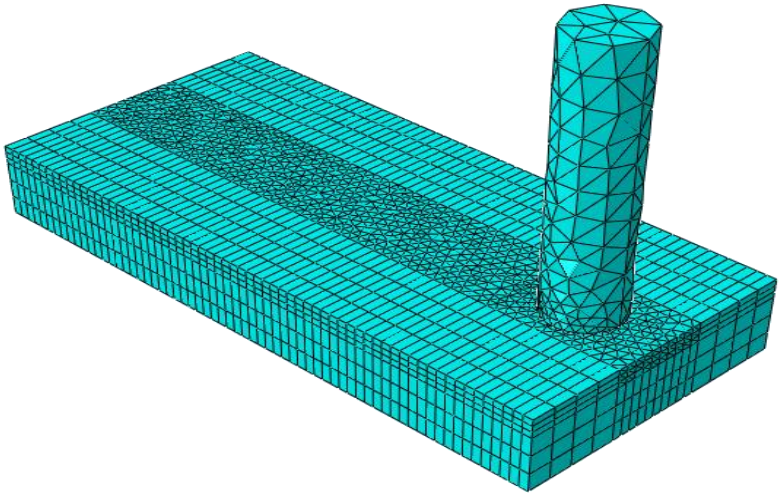

Figure 5.1 - First Lagrangian model

Another FE model was constructed to simulate the FSW process using Lagrangian formulation; the model was based on the previous Lagrangian model but was modified to minimize the computational cost. The rectangular plate with a starting hole was difficult to mesh as elements around the hole tended to have high aspect ratios. The problem was eliminated by changing the geometry, so that a uniform aspect ratio close to 1 was achieved around the middle hole. The plate geometry was, therefore, changed to a circular shape to achieve better meshing around the pin. The remeshing rules were also specified but with a lower frequency. Figure 5.2 shows the mesh density used for tool and the circular plate. The computational cost was successfully reduced, as it took less time than the previous model. However, the run was aborted at less than 10% of the process due to excessive element distortion and no valuable results could be extracted. Figure 5.3 shows the distorted elements around the starting hole which caused the model to abort.

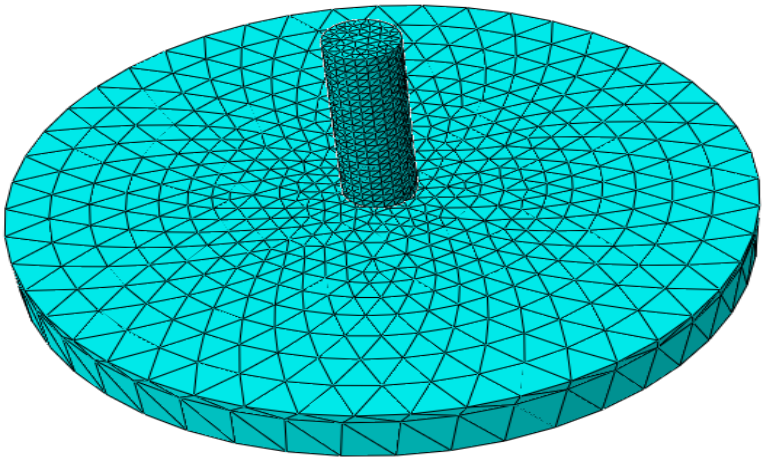

Figure 5.2 - Second Lagrangian model

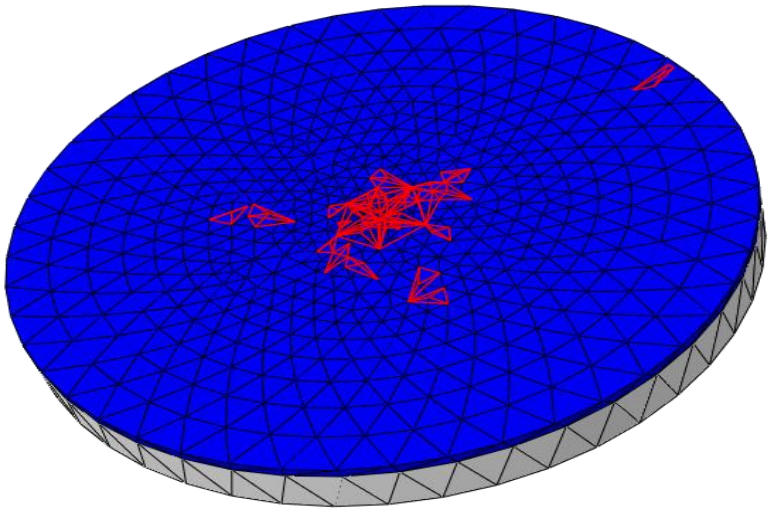

Figure 5.3 - Distorted elements around the starting hole in Lagrangian model

To overcome the above-mentioned difficulties, Eulerian-Lagrangian formulation was utilized in the present FE analysis to model the FSW process. The welding plate was modeled using Eulerian part definition whereas; a Lagrangian part was assigned for the welding tool. Eulerian definition allows the material to flow through the mesh while the elements stay stationary and unaffected during the process. Moreover, using Eulerian elements eliminates any mesh distortions that occur during the process. The plate geometry is identical to the plates used in the experimental work, yet the welding tool was modified for simplicity. The welding plate was 130 mm in length, 60 mm in width and 4 mm in thickness. As for the

welding tool, the diameter of the shoulder was 15 mm, and the diameters of the pin and length were 5 mm and 4 mm, respectively. The backing plate was removed from this model as merging any part with a rigid part is not allowed in the current Eulerian part definition in ABAQUS. Figure 5.4 show the geometric description of the FE model used in the present analysis. More details about the FE modeling are given in the following subsections.

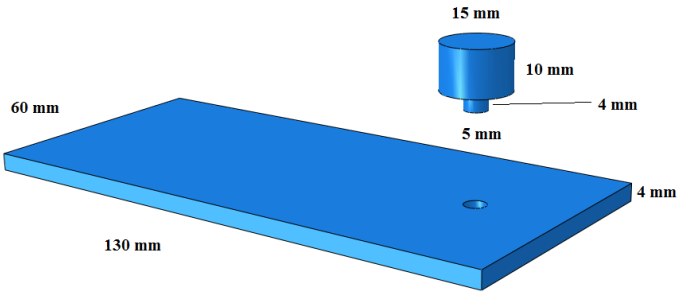

Figure 5.4 – Tool and plate geometry

5.2.1 Material definition

The rotating tool was made of very high strength steel and was defined using Lagrangian formulation in the present FE simulations. The thermal conductivity used for steel was 45 $\frac{W}{m \cdot K}$ with a specific heat of 0.49 $\frac{KJ}{Kg \cdot K}$. The welding plate was made of 5083 aluminum alloy with a density of 2650 $\frac{kg}{m^3}$ and an elastic modulus of 72 GPa. The thermal conductivity of the alloy was set to 121 $\frac{W}{m \cdot K}$ with a specific heat equal to 0.91 $\frac{KJ}{Kg \cdot K}$. The thermo-viscoplastic behavior of aluminum alloy was defined using the Johnson-Cook material and damage models available in ABAQUS. Table 5-1 summarizes the Johnson-Cook parameters for plasticity and damage evolution that were collected from the literature [45].

Table 5-1 - Johnson-Cook plasticity and damage evolution parameters [45]

Plasticity Parameters						
A	**B**	**C**	**m**	**n**	**T_m (K)**	**T_r (K)**
137890000	216730000	0.02	0.4845	1.225	933	293
Damage Evolution						
d_1	**d_2**	**d_3**	**d_4**	**d_5**	**T_m (K)**	**T_r (K)**
0.178	0.389	-2.246	0	0	933	293

5.2.2 Contact and boundary conditions

General contact definition was used to model the FSP process with a defined slipping condition. The maximum elastic slip used was 0.5% which is a default value defined by ABAQUS. The contact was defined in both normal and tangential directions of the plate. Hard contact definition was used in the normal direction and a penalty contact was adopted in the tangential direction, with a friction coefficient equal to 0.3 as recommended by previous research [41]. Heat generation due to friction was also defined and was distributed equally to each surface.

The bottom surface of the Eulerian welding plate was restrained from movement in all directions. A range of rotational speeds between 600 and 900 rpm was assigned to the tool, which was moving with a speed of 50 mm/min in the welding direction. The rigid tool was restrained from any rotation or movement in directions other than the previously specified. A predefined temperature field was also assigned to the welding plate and the tool to start the process at room temperature.

5.2.3 Mesh description

A total of 3200 elements were initially utilized to model the welding plate using 8-node 3D solid elements as shown in Figure 5.5b. Adaptive Eulerian-Lagrangian (ALE) meshing technique, which is very important for large deformation modeling, was also adopted to prevent any elements distortions during the process. When using Eulerian elements, a percentage of material is specified to fill each element. If the elements are set to 100% material, no room would be left for the material to move in the elements during the deformation causing a distortion to occur. On the other hand, setting the elements to less than 100% material will reduce the amount of material per element and in the whole part which creates voids between the elements making the model unrealistic. ALE technique allows the elements to start with 100% material and changes the percentage of material per element as the process goes on which allows the material to stir without causing any distortions or fictitious voids [44].

Mesh sensitivity analysis was initially conducted to select a proper element size to accurately simulate the FSW process with a minimum computational cost. In this regard, three mesh sizes were considered, coarse mesh (Mesh A), fine mesh (Mesh B) and very fine mesh (Mesh C) as shown in Figure 5.5. The peak temperatures obtained using these three meshes were compared with the experimental values as illustrated by the bar char shown in Figure 5.6. FE modeling using Mesh A was found to overestimate the experimental peak temperature at the thermocouple location by more than 18%. On the other hand, the peak temperatures predicted using Mesh B and Mesh C were comparable with their experimental counterparts with a maximum difference of less than 4%. Mesh B was; therefore, selected in this study as it requires less computational time than Mesh C with acceptable accuracy.

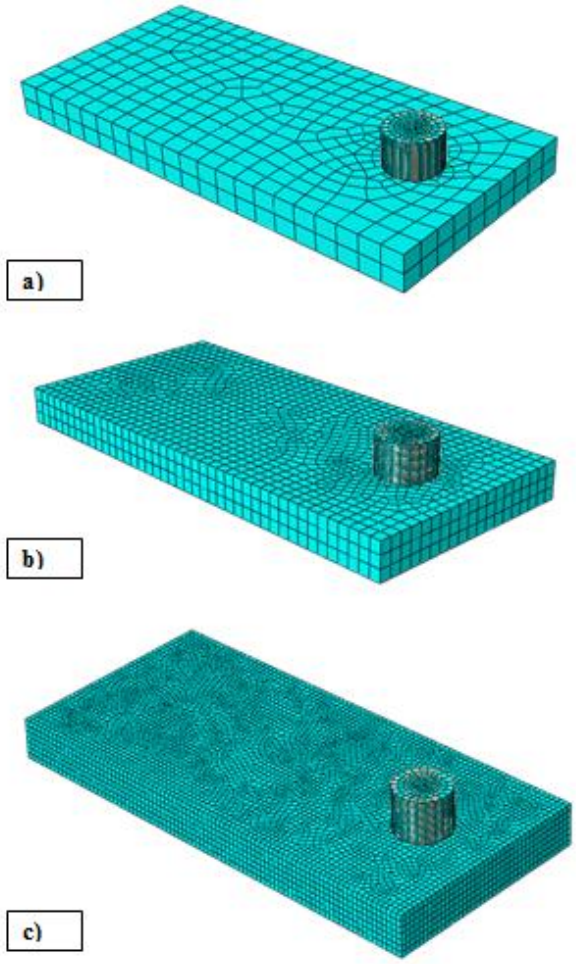

Figure 5.5 – Three mesh sizes tried (a) coarse mesh, (b) fine mesh (used), and (c) very fine mesh

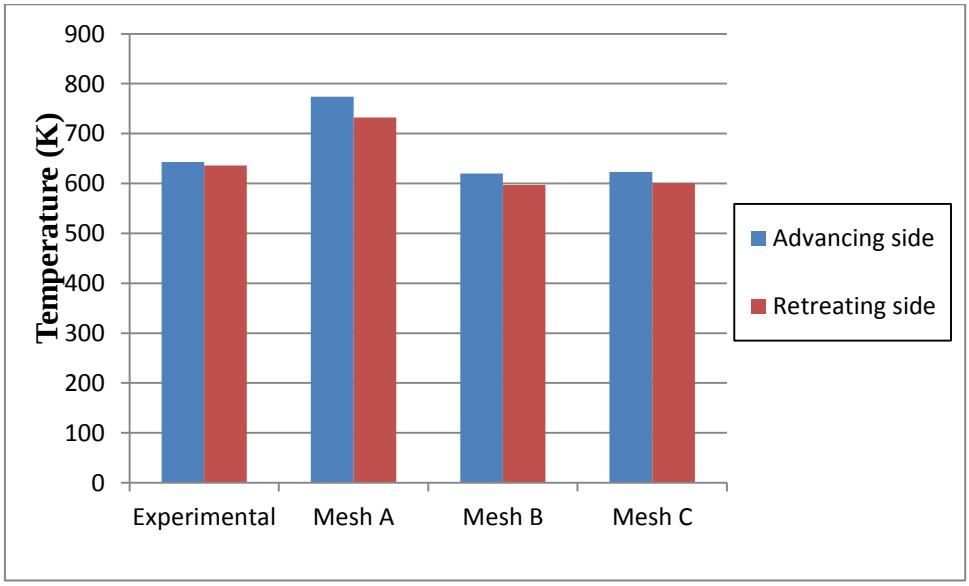

Figure 5.6 - Peak temperatures at the three different mesh sizes

5.4 FE Results and Validation

The present FE model was verified against experimental results for a FSW sample with similar conditions. The comparisons between the experimental results and the present numerical analysis included (a) the peak temperatures obtained at different rotational speed, (b) the difference in temperatures between the advancing and retreating sides, and (c) the thermal profile captured by the Infra-red camera.

The FE model was run at three different rotational speeds; 600 rpm, 700 rpm and 900 rpm. The resulting peak temperatures and thermal profiles encountered at these three speeds were compared with the results obtained from the experiments. Figure 5.7 presents the variation of the peak temperatures with the rotational speeds as recorded from the experiment and the numerical simulation. The FE model successfully predicted the temperature profiles of FSP at the three different rotational speeds. The peak temperature predicted by the FE model compared well with the experimental values at the first two rotational speeds, but it was slightly overestimated as the rotational speed increased. Nonetheless, the difference between the temperatures in the advancing and retreating sides was very close to the experimental results in all three rotational speeds. At 600 rpm, the peak temperature predicted by the model was 5% lower than the temperature found experimentally. The differences in the peak temperatures between the advancing and retreating sides obtained experimentally and numerically were identical. When the rotational speed is increased to 700 rpm, the peak temperature values predicted by the FE model were closer to the experimental values. The difference in the temperatures predicted by the FE model was around 3.6% in the advancing side and 4.5% in the retreating side when compared to the experimental values. Also, the FE model predicted a larger gap between the advancing and retreating side at this welding condition. When the rotational speed increased to 900 rpm, there was noticeable difference in the peak temperatures where the values predicted by the FE model were higher than the experimental values. A large difference was seen between the advancing and retreating sides as well. The largest difference between the predicted and experimental temperatures was 8.5%. It should be noted, however, that the sample at the 900 rpm was overheated, and a flash mass of material was ejected outside the stir zone. Figure 5.8 shows the thermal profile at the three different rotational speeds. The three thermal profiles are similar where the advancing side achieved higher temperatures

than the retreating side. The figure also shows the increase in the overall temperature in addition to the peak temperatures as the rotational speed increases. The increase of heat generated is due to the increase of friction caused by raising the rotational speed of the tool.

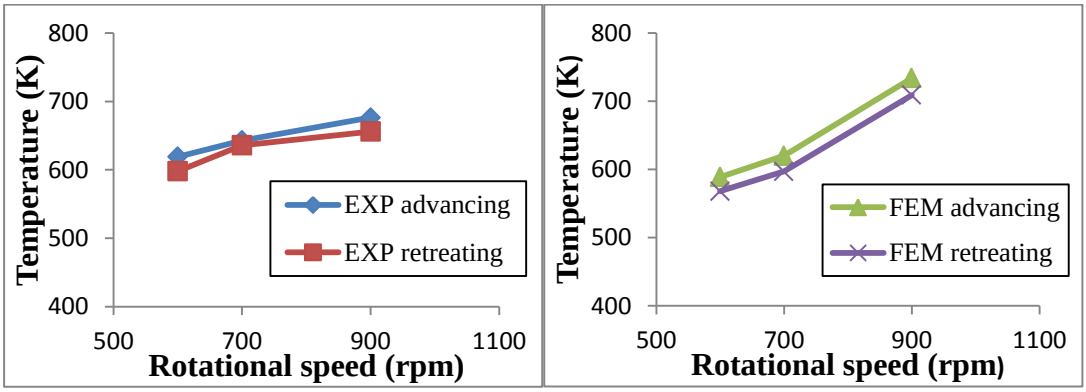

Figure 5.7 - Peak temperatures at the advancing and retreating sides found from experiments (left) and numerical model (right)

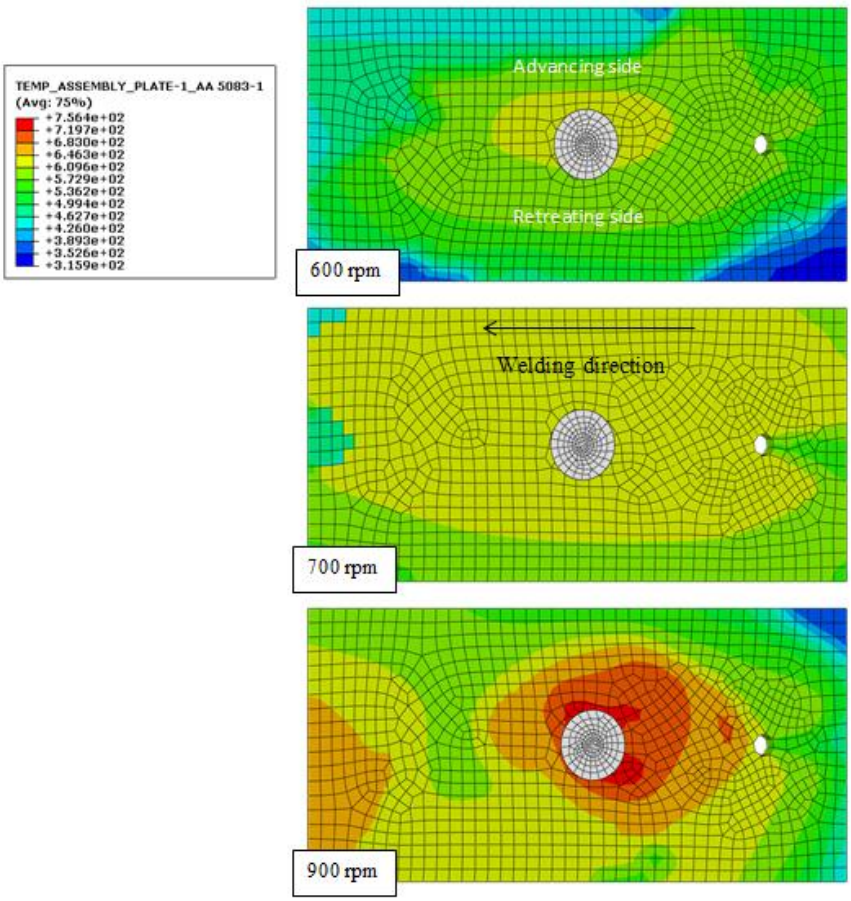

Figure 5.8 - Thermal profiles of FSP samples at 600 rpm (top), 700 rpm (middle) and 900 rpm (bottom)

Infrared images of FSP were also taken during the experiment to show the temperature profile at different locations over the specimen. Samples of these images taken at two different locations are presented in Figure 5.9 for the case of a rotational speed equal to 700 rpm. The FE model was able to predict similar temperature profiles to the ones captured by the IR camera for the same rotational speed as depicted in Figure 5.10. The IR camera images were limited to a small diameter surrounding the tool as parts of the plate were hidden by the clamps holding it in the test setup. One advantage of the FE modeling is that the temperature profile can be observed over the whole plate which gives a better understanding of the thermal profile evolution during the FSP. As was expected from the results discussed previously in this chapter, the advancing side achieved higher peak temperature than the retreating side. As the tool is rotating and moving in the welding direction, the rotation of the tool acts in the same direction of the weld in the advancing side, while it acts in the opposite direction of the weld in the retreating side. This movement causes the temperature in the advancing side to increase further and the material to be moved from the retreating to the advancing side. Figure 5.11 shows a FSP sample with excess material appearing on the advancing side with an indication of the weld direction and rotational direction.

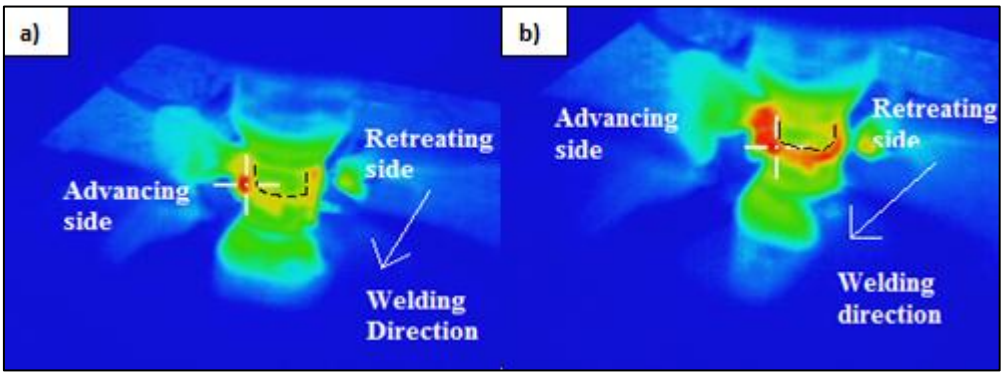

Figure 5.9 - Thermal profile captured by infrared camera at (a) beginning of FSP (b) halfway through FSP

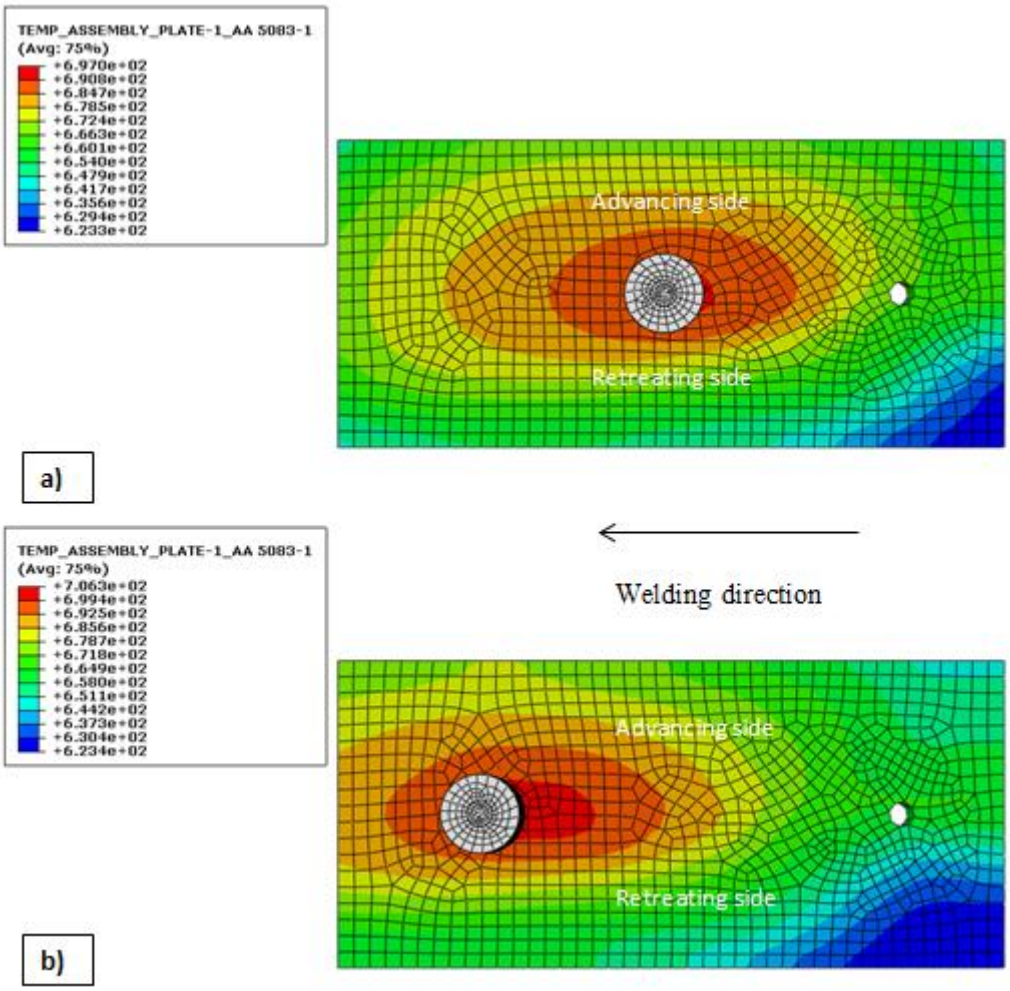

Figure 5.10 - Thermal profile predicted by FE model at (a) halfway through FSP and (b) end of FSP

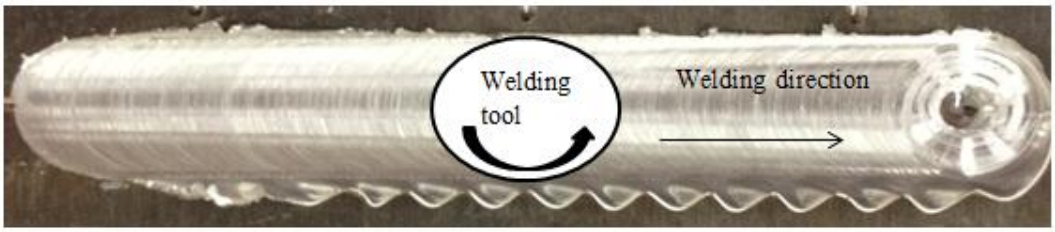

Figure 5.11 - FSP sample showing excess material in advancing side and rotational and welding direction of the tool

Chapter 6 : Summary and Future Work

Friction stir welding is a relatively new welding technique which can be easily used to achieve high quality welds in aluminum alloys compared to other welding techniques. The welding is controlled by different parameters, such as tool rotational speed, feed rate and welding medium. Controlling the welding parameters in in-air FSW helps to improve the mechanical and microstructural properties of the welded material. The findings of this study can be summarized as follows:

(1) Submerged friction stir welding was successfully used to produce weld with good tensile and microstructural properties compared to parent material.
(2) Controlling the process parameters is very crucial in controlling the resulting properties of the weld.
(3) Submerging was found to decrease the heat input during welding which limits the grain growth during the welding process. The decrease in heat input resulted in reducing the microscopic voids in the material leading to an increase in microhardness and improvement of tensile properties.
(4) The increase in rotational speed caused an escalation in heat input due to friction. It was found that good weld properties can be achieved at the relatively low rotational speed possible; however, very low rotational speeds could also result in improper stirring and thus formation of void defects.
(5) The feed rate plays a crucial role in controlling the heat input into the welded sample as well. The increase in feed rate was proven to slightly increase the peak temperature but reduce the processing time. The reduction in processing time also means a reduction in the time which heat is applied to the welding sample; thus, this limits the grain growth.
(6) The power consumption during the welding process was found to be affected by submerging conditions as less power was consumed during submerged FSW. On the other hand, increasing the rotational speed was proven to increase the power consumption; whereas, increasing the feed rate was found to decrease the total energy spent during the welding process.

(7) The FSW process was found difficult to model using Lagrangian finite element formulation as the high plastic deformation caused an excessive distortion in the mesh. Overcoming this issue was attempted by using a very fine mesh as well as remeshing techniques. However, the computational time increased drastically.
(8) Finite element simulation of the FSW process was successfully achieved by adopting the Eulerian formulation. The peak temperatures in the advancing and retreating sides in addition to the thermal profiles were successfully predicted and validated using the experimental results.

Future work and recommendations:

(1) Further microstructural investigation could be conducted to study factors like grain growth and precipitation during in air and submerged FSW.
(2) Further investigation on submerged FSW can be conducted at different water temperatures. Additionally, other coolants could be used to further control the grain growth in the process.
(3) Other cooling strategies, such as adding an inflow and outflow of coolant during the welding process, could be used.
(4) A backing plate with higher heat conduction can also be introduced to increase the cooling rate in Submerged FSW.
(5) The FE model could be expanded to include the effect of different submerging conditions on FSW. The microstructure of the welded material can also be predicted by using the Zener-Hollomon relation.

References

[1] W.M. Thomas, E.D. Nicholas, J.C. Needham, M.G. Murch, P. Temple Smith, and C.J. Dawes, "Friction stir butt welding," International patent application No. PCT/GB92/02203; December 1991.

[2] R.S. Mirsha and Z.Y. Ma, "Friction stir welding and processing," *Materials Science and Engineering*, 2005.

[3] M. Peel, A. Steuwer, M. Preuss and P.J. Withers, "Microstructure, mechanical properties and residual stresses as a function of welding speed in aluminum AA5083 friction stir welds," *Acta Materialia*, 51, pp 4791–4801, 2003.

[4] K. V. Jata, K. K. Sankaran and J. J. Ruschau, "Friction-stir welding effects on microstructure and fatigue of aluminum alloy 7050-T7451," *Metallurgical and Materials Transactions*, 31, pp.2181-2192, 2012.

[5] H.J. McQueen, M. Cabibbo, E. Evangelista, S. Spigarelli, M. Di Paola, and A. Falchero, "Microstructure and mechanical properties of AA6056 friction stir welded plate," *Metallurgical Science and Technology*, pp. 22-30, 2007.

[6] W.B. Lee, Y.M. Yeon, and S.B. Jung, "The improvement of mechanical properties of friction-stir-welded A356 Al alloy," *Materials Science and Engineering*, A355, pp. 154-159, 2003.

[7] D. Klobčar, L. Kosec, A. Pietras, and A. Smolej, "Friction-Stir Welding Of Aluminium Alloy 5083," *Materials and Technology*, 46, pp. 483-488, 2012.

[8] M.A. Sutton, B. Yang, A.P. Reynolds and R. Taylor, "Microstructural studies of friction stir welds in 2024-T3 aluminum," *Materials Science and Engineering*, A323, pp. 160-166, 2002.

[9] J.A. Schneider, A.C. Nunes Jr., P.S. Chen and G. Steele, "TEM study of the FSW nugget in AA2195-T81," *Journal of Materials Science*, 40, pp. 4341-4345, 2005.

[10] J. Xu, S.P. Vaze, R.J. Ritter, K.J. Colligan, and J.R. Pickens, "Experimental and numerical study of thermal process in friction stir welding," in *Joining of advanced and and specialty Materials IV*, pp. 10-19, 2004.

[11] M.J. Jones, P. Heurtier, C. Desrayaud, F. Montheillet, D. Allehaux, and J.H. Driver, "Correlation between microstructure and microhardness in a friction stir welded 2024 aluminium alloy," *Scripta Materialia*, 52, pp. 693–697, 2005.

[12] J.R. Groza, J.F. Shackelford, E.J. Lavernia, and M.T. Powers, *Materials Processing Handbook*, Boca Raton, FL: CRC Press, 2007.
[13] R. Zettler, A.C. Blanco, J.F. Dos Santos, and S. Marya, "The effect of process parameters and tool geometry on thermal field development and weld formation in friction stir welding of the alloys AZ31 and AZ61," *Magnesium Technology TMS*, pp. 409-423. 2005.
[14] S. Hirasawa, H. Badarinarayan, K. Okamoto, T. Tomimura, and T. Kawanami, "Analysis of effect of tool geometry on plastic flow during friction stir spot welding using particle method," *Journal of material processing technology*, 210, pp. 1455–1463, 2010.
[15] H. Fujii, L. Cui, M. Maeda, and K. Nogi,"Effect of tool shape on mechanical properties and microstructure of friction stir welded aluminum alloys," *Materials Science and Engineering*, A 419, pp. 25–31, 2005.
[16] S. Adapa, T.P. Chu, and J.A. Schneider, "Evaluation of friction stir welds," in *ASME International Mechanical Engineering Congress and Exposition*, 2005.
[17] S.A. Khodir, T. Shibayanagi, and M. Naka, "Control of hardness distribution in friction stir welded AA2024-T3 Aluminum Alloy," *Materials Transactions*, Vol. 47, No.6, pp. 1560-1567, 2006.
[18] Y.G. Kim, H. Fujii, T. Tsumura, T. Komazaki, and K. Nakata,"Three defect types in friction stir welding of aluminum die casting alloy," *Materials Science and Engineering*, A 415, pp. 250-254, 2006.
[19] R. Leal and A. Louriero,"Defects formation in friction stir welding of aluminum alloys," *Materials Science Forum*, Vols. 455-456, pp. 299-302, 2004.
[20] P. Cavaliere, R. Nobile, F.W. Panella, and A. Squillace,"Mechanical and microstructural behaviour of 2024–7075 aluminium alloy sheets joined by friction stir welding," *International Journal of Machine Tools & Manufacture*, 46, pp. 588–594, 2005.
[21] Z.Y. Ma, S.R. Sharma and R.S. Mishra, "Effect of multiple-pass friction stir processing on microstructure and tensile properties of a cast aluminum–silicon alloy," *Scripta Materialia*, 54, pp. 1623–1626, 2006.
[22] L.B. Johannes and R.S. Mishra, "Multiple passes of friction stir processing for the creation of superplastic 7075 aluminum," *Materials Science and Engineering*, 464, pp. 255–260, 2007.

[23] J. Gandra, R.M. Miranda, P. Vilac¸, "Effect of overlapping direction in multipass friction stir processing," *Materials Science and Engineering*, 528, pp. 5592–5599, 2011.
[24] R. Brown,W. Tang, A.P. Reynolds, "Multi-pass friction stir welding in alloy 7050-T7451: Effects on weld response variables and on weld properties," *Materials Science and Engineering*, 513–514, pp. 115–121, 2009.
[25] H.J. Liu, Y.C. Chen, and J.C. Feng, "Effect of heat treatment on tensile properties of friction stir welded joints of 2219-T6 aluminium alloy," *Materials Science and Technology*, Vol 22 No.2, pp. 237-241, 2006.
[26] P. J. Konkol and M. F. Mruczek, "Comparison of Friction Stir Weldments and Submerged Arc Weldments in HSLA-65 Steel," *The Welding Journal*, 86, pp. 187-195, 2007.
[27] P. Upaghyay and A.P. Reynolds,"Effects of thermal boundary conditions in friction stir welded AA7050-T7 sheets," *Materials Science and Engineering*, A 157, pp 1537-1543, 2010.
[28] H.J. Zhang, H.J Liu, and L. Yu, "Microstructure and mechanical properties as a function of rotation speed in underwater friction stir welded aluminum alloy joints," *Material and Design*, 32, pp 4402-4407, 2011.
[29] R.D. Fu, Z.Q. Sun, R.C. Sun, Y. Li, H.J. Liu, and L. Liu, "Improvement of weld temperature distribution and mechanical properties of 7050 aluminum alloy butt joints by submerged friction stir welding," *Material and Design*, 32, pp 4925-4831, 2011.
[30] H.J. Liu, H.J. Zhang, Y.X Huang, and L. Yu, "Mechanical properties of underwater friction stir welded 2219 aluminum alloy," *Trans. Nonferrous Met. Soc. China*, 20, pp 1387-1391, 2010.
[31] R.S. Mishra, Z.Y. Ma, and I. Charit, "Friction stir processing: a novel technique for fabrication of surface composite," *Materials Science and Engineering*, A341, pp. 307-310, 2003.
[32] Y.J. Kwon, N. Saito, and I. Shigematsu, "Friction stir process as a new manufacturing technique of ultrafine grained aluminum alloy," *Journal Of Materials Science Letters*, 21, pp 1473–1476, 2002.
[33] B.M. Darras, M.K. Khraisheh, F.K. Abu-Farha, and M.A. Omar, "Friction stir processing of commercial AZ31 magnesium alloy," *Journal of Materials Processing Technology*, 191, pp. 77–81, 2007.

[34] B. Darras, E. Kishta, “Submerged Friction Stir Processing of AZ31 Magnesium Alloy,” *Material and Design*, 47, pp.133-137, 2013.
[35] J.R. Davis, *Corrosion of Aluminum and Aluminum Alloys*, Materials Park, OH : ASM International, 1999, pp. 1-23.
[36] P. Colegrove, H. Shercliff and R. Zettler, “A Model for Predicting the Heat Generation and Temperature in Friction Stir Welding from the Material Properties,” *Science and Technology of Welding & Joining*, 12, pp. 284-297, 2007.
[37] P. Colegrove and H. Shercliff, “Two-dimensional CFD modelling of flow round profiled FSW tooling,” *Science and Technology of Welding & Joining*, 9, pp. 483-492, 2004.
[38] J-H Cho, P. Dawson and D. Boyce, “2-D Modeling of Friction Stir Welding by Eulerian Formulation,” *AIP Conf. Proc.* 712, pp. 1326-1331, 2004.
[39] G. Buffa, J. Hua, R. Shivpuri, and L. Frantini, “A continuum based fem model for friction stir welding – model development,” *Material Science and Engineering*, A 419, pp. 389-396, 2005.
[40] Hamilton C., Sommers A., Dymek S., 2008, “A thermal model of friction stir welding applied to Sc-modified Al-Zn-Mg-Cu alloy extrusion,” *International Journal of Machine tools & Manufacture*, 49, pp. 230-238.
[41] Z. Zhang and H.W. Zhang, “Numerical studies on controlling of process parameters in friction stir welding,” *Journal of materials processing technology*, 209, pp. 241–270, 2009.
[42] H. Schmidt and J. Hattel, “A local model for the thermomechanical conditions in friction stir welding*,” Modelling and Simulation in Materials Science and Engineering*, 13, pp. 77-93, 2005.
[43] D.C. Hofmann, and K.S. Vecchio, "Submerged friction stir processing (SFSP): An improved method for creating ultra-fine-grained bulk materials," *Materials Science and Engineering A*, 402, pp 234-241, 2005.
[44] ABAQUS/CAE Analysis User's Manual: version 6.11 (2011) by Abaqus.
[45] I. Polyzois, “Finite Element Modeling of the Behavior of Armor Materials Under High Strain Rates and Large Strains,” M.Sc. Thesis, University of Manitoba, Canada, 2010.
[46] M. Khraisheh, B. Darras, P. Kalu, M. Adams-Hughes and N. Chandra, “Correlation between the Microstructure and Forces Generated during Friction Stir Processing of AA5052”, Mater. Sci. Forum 475-479, 3043-3046, 2005.

[47] B. Darras, M. Omar, M. Khraisheh, "*Experimental Thermal Analysis of Friction Stir Processing*", Mater. Sci. Forum 539-543, 3801-3806, 2007.

[48] A. Denquin, D. Allehaux, M.H. Compagnac, and J. Lapasset, "Relationship between microstructural variations and properties of friction stir welded 6056 aluminium alloy," *Welding in the world*, 46, pp. 14-19, 2002.

[49] Y. S. Sato, M. Urata, H. Kokawa and K. Ikeda, "Hall-Petch relationship in friction stir welds of equal channel angular-pressed aluminium alloys," *Material Science and Engineering*, 354, pp. 298-305, 2003.

[50] Y. S. Sato, H. Kokawa, M. Enomoto, and S. Jogan, "Microstructural evolution of 6063 aluminum during friction-stir welding," *Metallurgical and Materials Transactions*, 30 , pp 2429-2437, 1999.

[51] K. Elangovan, and V. Balasubramanian, "Influences of pin profile and rotational speed of the tool on the formation of friction stir processing zone in AA2219 aluminium alloy," *Materials Science and Engineering*, A 459, pp. 7–18, 2007.

[52] Aalco, "Aluminium Alloys - Aluminium 5083 Properties, Fabrication and Applications, Supplier Data by Aalco," Internet: http://www.azom.com/article.aspx?ArticleID=2804, Jul. 16, 2013 [Oct. 12, 2013].

[53] G. Liu, S. Scudino, R. Li, U. Kuhn, J. Sun and J. Eckert, "Coupling effect of primary voids and secondary voids on the ductile fracture of heat-treatable aluminum alloys," *Mechanics of Materials*, 42, pp. 556 – 566, 2011.

[54] S. Almeida and Z. Neto, "Effect of void content on the strength of composite laminates," *Composite Structures*, 28, pp. 139 – 148, 1994.

Vita

Emad Eldin Kishta was born on September 25th, 1989, in Abu Dhabi, United Arab Emirates. He received his high school diploma from Al-Nahda National School in Abu Dhabi in 2007. He graduated from the American University of Sharjah in 2011 with a Bachelor's degree in Mechanical Engineering. Then, Emad joined the Master of Science in Mechanical Engineering program in the American University of Sharjah. He received a full scholarship and worked as a graduate research and teaching assistant. During his graduate studies, he published an article with his thesis advisor in Materials and Design Journal.